POLITECNICO DI TORINO

Collegio di Ingegneria Chimica e dei Materiali

Master of Science Course in Chemical and Sustainable Processes Engineering

Politecnico di Torino

Master of Science Thesis

CFD simulation of gas-solid hydrodynamics in a high-pressure fluidized bed

Tutor:
Daniele Marchisio

Candidate:
Simone Chiarla

Marzo 2024

Abstract

Fluidized bed gasifiers have emerged as a prominent technology for the thermal conversion of biomass. This process reflects a green solution for producing combustible fuel gas or biopower, thus contributing to energy security within the modern energy system. Moreover, high-pressure gasification is viewed as beneficial, facilitating a more effective integration with processes downstream.

This study presents the hydrodynamic analysis of a pilot-scale pressurized fluidized bed gasifier, at a cold-flow status, performed using CFD tools. The analysis is carried out building a 3D geometry of the reactor and employing the Eulerian model with the kinetic theory of granular flows to describe gas-solid interactions. The system's behaviour is investigated by examining the influence that operational conditions, such as operating pressure, fluid inlet velocity, and particle size distribution, have on it.

The results show how an increase in operating pressure and inlet velocity makes the gas-solid system more homogeneous, thus promoting the reactions occurring at the operating temperature. Furthermore, a higher gas inlet velocity also ensures a reduced gas bypass, a phenomenon that is more pronounced with an increase in operating pressure. In both scenarios, an increase in pressure drop is observed. Additionally, higher operating pressures require more precautions to ensure the structural stability of the reactor.

On the other hand, an increase in the diameter of solid particles leads to a worse mixing quality inside the reactor and a pronounced gas bypass. Moreover, considering the range of sizes analysed, larger sand grains also result in increased pressure losses.

Finally, the study aims to assess the fluidization regime of all cases examined. Given the high gas velocities targeted for operation, the systems exhibit highly turbulent fluidization regimes with a significant transport of solid particles.

Prefazione

Simulazione CFD dell'idrodinamica gas-solido in un letto fluido ad alta pressione

I gassificatori a letto fluido risultano essere una tecnologia di spicco per la conversione termica della biomassa, nonché una potenziale soluzione green per la produzione di gas combustibile ed energia elettrica pulita. Inoltre, la gassificazione ad alta pressione è considerata vantaggiosa, data la facilità di integrazione con i processi a valle.

Questo studio presenta l'analisi idrodinamica di un gassificatore pilot-scale a letto fluido pressurizzato, in uno stato cold-flow, eseguita utilizzando strumenti CFD. L'analisi è condotta costruendo una geometria tridimensionale del reattore e impiegando il modello Euleriano, accoppiato con la teoria cinetica dei flussi granulari, per descrivere le interazioni gas-solido. Il comportamento del sistema è investigato esaminando l'influenza che le condizioni operative, in particolare la pressione operativa, la velocità di ingresso del fluido e la granulometria delle particelle, hanno su di esso.

I risultati mostrano come un aumento della pressione operativa e della velocità di ingresso del gas renda il sistema gas-solido più omogeneo, promuovendo così le reazioni che avvengono alla temperatura di esercizio. Inoltre, una maggiore velocità di ingresso del gas assicura anche un minore bypass di gas, fenomeno che risulta più marcato con un aumento della pressione operativa. In entrambi gli scenari, si osserva un aumento delle cadute di pressione. Inoltre, pressioni operative più elevate richiedono più precauzioni per garantire la stabilità strutturale del reattore.

D'altro canto, un aumento del diametro delle particelle solide porta a una peggiore qualità di miscelazione all'interno del reattore e a un bypass di gas più pronunciato. Inoltre, considerando le dimensioni delle particelle analizzate, grani di sabbia più grandi risultano comportare anche un aumento delle perdite di pressione.

Infine, lo studio mira a valutare il regime di fluidizzazione di tutti i casi

esaminati. Date le elevate velocità del gas, di interesse per il funzionamento del reattore, i sistemi mostrano regimi di fluidizzazione altamente turbolenti con un notevole trasporto di particelle solide.

Contents

List of Figures

List of Tables

Chapter 1

Introduction

Since the Industrial Age, the world economy and energy system has always been based mainly on the extraction and use of fossil fuels. It is thanks to resources such as coal, oil, and natural gas, that it has been possible to shape modern society as it is known today. However, the dramatic consequences that the intensive exploitation of these non-renewable sources entails have long been a topic of debate for politics and the scientific community. One of the most frightening data certainly concerns global warming. According to the World Meteorological Organization (WMO), the chance of temporarily reaching the 1.5°C threshold set in the Paris Agreement by 2026 is equal to 50% [1].

To alleviate the consequences of climate change, that are already taking place in many countries of the world, numerous initiatives have been taken. A clear example is the European Green Deal, a package of proposals and actions that embodies the EU's strategy to face the green transition, with the aim of climate neutrality by 2050 as the ultimate goal [2]. The recent conflict in Ukraine has increased the need for European countries to adopt more sustainable energy alternatives in the short term. The desire on the part of member countries to become independent from Russian fossil fuels is embodied in the REPowerEU: a plan born with the purpose of diversifying renewable energy sources and taking decisive steps towards green technologies [3]. To achieve these goals, various companies started changing the way they interpret industry, agriculture, or transport.

Looking at the potential of new energy sources, a primary role is covered by biomass, i.e., organic matter derived from animals and plants, available in a renewable basis [4]. The International Energy Agency (IEA) [5] provides a comprehensive picture of what bioenergy is today and what its developments may be in the future. This green energy accounts for 55% of the total renewable energy produced worldwide and covers 6% of global needs. The

use of biomass is still mainly linked to heating purposes, but in a Net Zero scenario it will play an important role in all those sectors that are difficult to electrify, like shipping and aviation.

Starting from the general definition of *biomass*, it is possible to classify different types of raw materials by this label. This category encompasses both virgin biomass, such as ligno-cellulosic compounds (wood, plants) and carbohydrate-based materials (vegetables, crops), and less noble materials, such as municipal solid waste, sewage, and other agricultural waste [6].

Due to its diversity and availability, biomass can be transformed into valuable products through a wide range of different processes. Of all the biomass-to-energy conversion technologies, gasification is certainly one of the most attractive ones. Among the advantages of this thermo-chemical process, it is worth mentioning the ability to accept a wide variety of inputs, like wood, crop, sewage and agricultural residues, which otherwise would have been unused and dumped in landfills [7]. In addition, gasification represents a well-proven technology as it has traditionally been used for decades for the production of syngas and char from coal [8]. Finally, a further advantage lies in the preciousness of the products themselves. The solid component can be used as fertilizer, while the synthesis gas contains the building blocks of valuable chemicals and fuels. In particular, syngas represents one of the main sources of hydrogen and a raw material for the production of second-generation biofuels, like methanol and Fischer-Tropsch (FT) fuels. As an alternative, it can also be directly burned at high temperatures, to produce power and heat, resulting in a lower release of pollutants than conventional biomass combustion. [7, 9].

1.1 Bio-FlexGen project

In this scenario, the Bio-FlexGen project takes place. This EU-funded initiative has the aim of developing an efficient and flexible combined heat and power plant (CHP) system by using green hydrogen and biomass to give a contribution in the decarbonization of the energy system [10]. The project is carried out by a consortium of 14 partners, located in 5 different countries of the European Union. The Bio-FlexGen project's partners include Phoenix BioPower, a company that is leading the pursuit of sustainable energy solutions and is in charge of the development of BTC (Biomass-Fired Top Cycle) technologies.

The heart of the project is the development of a high-pressure gasification plant capable of synthesizing syngas from biomass. The input of the

process collects all those agricultural and forestry wastes with a great potential from the point of view of energy valorization. The gas produced by the gasification process is cooled down and filtered before being burned. After the combustion process, the flue gases are then sent to a turbine with the purpose of generating electricity with an efficiency up to 60%, the double compared to a turbine in a conventional biomass plant. The flexibility of the plant lies in the ability of the gas turbine combustion system of handling combustible gases characterized by always different compositions. The waste heat of the gases coming out of the turbine is recovered in the form of steam, which is partly used for the gasification process and partly distributed to the surrounding towns for district heating. Finally, carbon dioxide is captured and stored in order to have a negative-emission process.

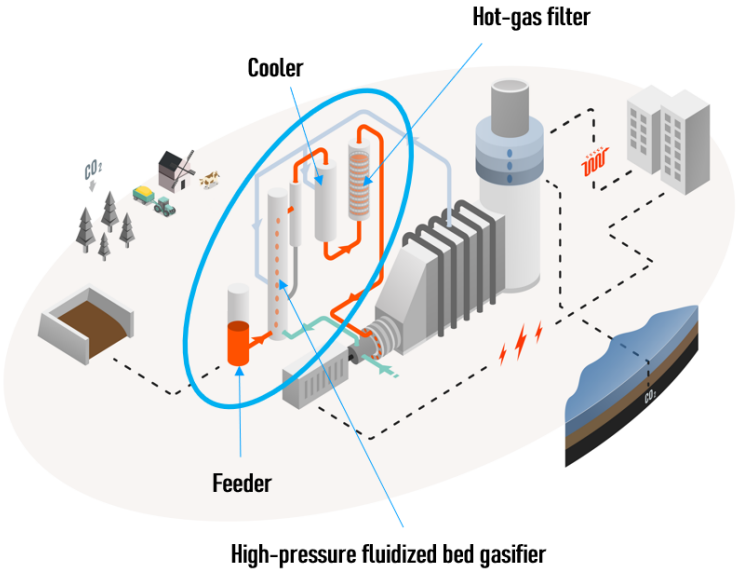

Figure 1.1: Phoenix BioPower Biomass-Fired Top Cycle plant [10].

This work will use the software Ansys Fluent, version 2023 R2, to simulate gas-solid interactions in a pilot-scale pressurized fluidized bed gasifier, in orded to capture hydrodinamics characteristics in high-pressure conditions. In addition, the study will aim to investigate the effect of operating pressure, gas inlet velocity, and particles granulometry on the general behavior of the system of interest. The study will be carried out at the Department of Chemical Engineering and Technology at KTH, in close collaboration with Phoenix BioPower, two of the fourteen partners of the Bio-FlexGen consortium.

Chapter 2

Technical Aspects of Biomass Gasification

2.1 Biomass

As already mentioned, gasification is a process capable of accepting multiple types of biomass as inputs. However, depending on the chemical and physical characteristics of the raw material, the gas produced will take on a different composition, as well as the operating conditions will have to be adjusted on a case-by-case basis.

Dahlquist et al. [11] offer an overview of what are the properties of interest of biomass, in order to predict the quality of the synthesis gas and the operating conditions under which it is best to run the process. Focusing on the physical and thermodynamic features of potential feedstocks, a first property of interest is density, which can vary from 100 kg/m^3 of agricultural residues to 1200 kg/m^3 of dense and durable wood. Thermal conductivity and permeability to gas flow also play a key role in what the outcome of the process will be. Due to the anisotropic nature of biomass, these properties vary not only from material to material, but also take on different values when evaluated tangentially or perpendicularly to fiber bundles. Furthermore, thermal conductivity also depends on factors such as the porosity of the fuel, its moisture content, and the operating temperature. These variables, along with the ignition temperature of the fuel, have an impact on another thermodynamic property of interest, namely specific heat.

Shifting the focus to the chemical properties of the fuel, the energy content and chemical composition of the chosen sample are of primary importance for the outcome of the gasification process. Biomass is mainly composed of cellulose, hemicellulose and lignin, and the percentages of these organic

compounds vary between different raw materials. According to Mohan et al. [12], the pyrolysis chemistry of these compounds is significantly different from each other, and the different products synthesised during the thermochemical conversion affect the final composition of the gaseous output. In addition, the initial composition of the starting fuel also affects the quantity and chemistry of the by-products generated. The review on biomass gasification, published by Molino et al. [13], provides interesting data in that sense. The researchers collected the results of experiments conducted from different types of biomass and with a main focus on the production of tars. This term refers to those heavy hydrocarbons that are produced during the pyrolysis step of the gasification process and that condense at temperatures lower than the operating temperature. Monitoring the amount of tars produced is of primary importance as the cleaning of syngas involves the implementation of expensive and complex purification systems downstream the gasifier. It has been shown that a higher percentage of cellulose and hemicellulose leads to a higher concentration of heavy oxygenated organic compounds, while lignin is the precursor of tars with an aromatic structure.

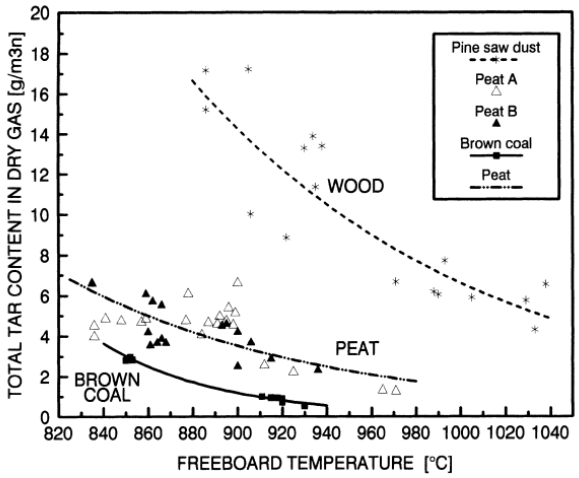

Figure 2.1: Tar concentrations for different feedstocks as a function of gasification temperature. [14]

It is not the intention of this thesis to delve into the complex chemistry behind the formation of compounds considered as the Achilles' heel of gasification, but it is important to underline how the quantity of these by-products can at least be minimized through precautions. Indeed, the conversion of biomass to tars depends on multiple other factors, including the moisture content of the fuel, the reactor configuration used, and the operating conditions that can be adjusted accordingly [9, 11].

Fuel (wood)	Updraft	Downdraft	Crossdraft
Moisture wet basis [%]	<60	<25	10–20
Dry-ash basis [%]	<25	<6	0.5–1.0
Ash melting temperature [°C]	>1000	>1250	
Fuel size [mm]	5–100	20–100	5–20
Application range [MW]	2–30	1–2	
Gas exit temperature [°C]	200–400	700	1250
Tar [g/Nm^3]	30–150	4.5–5.0	4.0–4.5
Gas *LHV* [MJ/m^{3}N]	5–6	85–90	75–90
Hot-gas efficiency [%]	90–95	3–4	2–3

Figure 2.2: Comparison of tars production in three fixed bed gasifier technologies. [15]

In order to optimise the gasification process, the biomass undergoes a series of pre-treatments before being utilized. Firstly, size reduction is required to obtain a homogeneous product suitable for gasification operations. Afterwards, biomass is sent to a drying process which makes a fuel characterised by a higher energy content and improved thermodynamic properties [13]. Indeed, a higher energy dissipation would happen in the presence of a more humid biomass. Higher heat dissipation results in a lower operating temperature, which in turn results in higher tars synthesis [9].

The drying process is often followed by a pelletization unit. The task of this unit is compressing the biomass, after having reduced it into sawdust with a grinding process, in order to produce small, smooth and cylinder-shaped pellets. This operation allows to obtain a product with a high volumetric energy content, high density, low moisture content and mechanically durable. The higher the dry density of the biomass, the higher the thermal conductivity. Finally, the use of pellets meets the needs of a continuous process, automatically fed and with fine calibration [16].

2.2 Gasifying agent

As a second reactant, gasification requires the use of an oxidizing agent for the thermo-chemical conversion of biomass into synthesis gas. The most widely used gasifying agents are air, steam, oxygen, and combinations of them [11, 17]. The mass flow rate of oxidizing agent sent to the gasifier plays an important role in the success of the process. Taking air as an example, a fuel/air ratio of about 6:1 would lead to the complete combustion of pellets. Therefore, in order to gasify biomass, it is necessary to operate with ratios of about 1.5:1, while remaining within the range of partial combustion [18]. Focusing on the different options available, the choice of the gasifying

medium has an impact on the quality of the final product, both in terms of composition and heating value.

	Air	Oxygen	Steam
Gas heating value, MJ/Nm^3	Low 4-6	High 10-15	High 15-20
	CO H_2 water, CO_2, HC Tar, N_2	CO, H_2, HC, CO_2,	
Average producer gas composition	H_2 – 15%, CO – 20%, CH_4 – 2%, CO_2 - 15%, N_2 - 48%,	H_2- 40%, CO – 40%, CO_2- 20%,	H_2 – 40%, CO -25%, CH_4 – 8%, CO_2-25%, N_2:2%,
Reactor temperature, °C	900 -1100	1000 -1400	700 -1200
Cost	Low	High	Medium

Figure 2.3: Comparison of syngas characteristics using different gasifying agents [19]

Air is a viable alternative due to its abundance, availability and its very low cost. However, the disadvantages are a high nitrogen content in the product gas and, as a consequence, a syngas with a heating value of 3-7 MJ/Nm^3 [11, 17],.

On the other hand, the use of pure oxygen lead to the production of a synthesis gas characterised by a much higher heating value, in the range of 12-28 MJ/Nm^3. Moreover, it would be possible to reach a higher carbon conversion, a low tars content and a remarkable purity in terms of H_2, CO and CH_4 [17]. The most intuitive disadvantage is the high cost due to separating oxygen from nitrogen using an air separation unit [17].

In this scenario, steam is an excellent alternative to produce a good quality synthesis gas at low cost. Through the use of steam, low tars production and high carbon conversion are guaranteed. In addition, due to the chemical structure of water, a hydrogen-rich syngas would be produced, characterised by a heating value of 10-18 MJ/Nm^3 [11, 17].

The BTC plant developed by Phoenix BioPower uses a mixture of air and oxygen as gasifyng medium. Steam is generated thanks to the hot exhaust gases from the gas turbine and it is partially sent to the gasifier. However, for the hydrodynamic studies to be carried out, an air-only stream will be considered as a gaseous supply to the reactor, in order to simplify the CFD simulation.

2.3 Gasification technology

Several reactor configurations have been developed over the decades to meet the different needs of industrial sites. A single gasification technology is not able to cover the entire wide range of applications. Indeed, it is possible to mention technologies which are more suitable to handle less treated biomass, as well as configurations which may be preferable for either small or large scale. According to Dahlquist et al.[11], a first distinction may be done looking at the relative motion between the gaseous and the solid phase and the bulk density of the solid.

Moving or fixed bed gasifiers are defined as reactors in which the fuel is supported by a grate and moves down the gasifier in the form of a plug. This reactor configuration is suitable for small scale operations, being able to produce energy in the range 10 kW-10 MW, and, depending on the position of the gas inlet, can be further divided into subgroups. In particular, downdraft, updraft and cross-draft gasifiers are the most common types of reactors belonging to this category.

For the development of the BTC plant, the member companies of the Bio-FlexGen project focused on the development of a fluidized bed gasifier, i.e., a reactor where the gas stream is sent to the bottom of the vessel and is forced through the bed particles. The solid phase, at a sufficiently high gas velocity, acquires a fluid-like behaviour. Depending on the gas velocity magnitude, a distinction can be made between bubbling fluidized bed (BFB) gasifiers and circulating fluidized bed (CFB) gasifiers, which are both described in depth in the following paragraphs.

One of the most appreciated features of fluidized beds is the high mixing degree, improved by the addition of inert particles to the reactive solid phase. Good mixing results in high heat and mass transfer, which in turn guarantees high reaction rates and an almost uniform temperature inside the reactor [11]. Uniform conditions are achieved thanks to the hydrodynamics of this technology, characterised by the presence of gas bubbles that continuously stir the solid particles [13]. Other strengths of this reactor configuration are the ability to process fuels with high moisture content and different compositions, the high carbon conversion, up to 98%, and the possibility of being able to use catalysts to lower the tars content [17, 18]. Moreover, the good ability to scale-up makes fluidized bed reactors suitable for large scale operations, ensuring a higher energy production compared to fixed bed gasifiers [13]. However, there are also some flaws in this technology, such as restrictions on the maximum operating temperature. Both BFB and CFB gasifiers should not operate at temperatures higher than the ash melting point to avoid defluidization phenomena of the bed. This limit leads to further consequences

which affects the costs of the overall process. Relatively low temperatures, coupled with short gas residence times, do not allow reaction rates to reach chemical equilibrium. This is reflected in a high percentage of methane in the gaseous product and a medium quantity of tars in the syngas, which requires a careful cleaning downstream the gasification [11]. Erosion of the gasifier walls is another drawback of fluidized bed technology, mainly for CFB gasifiers, as well as the costs required to install a gas filter at the outlet of the reactor [20]. In this specific case, this additional unit prevents the particles transported by the gaseous stream from seriously damaging the blades of the gas turbine.

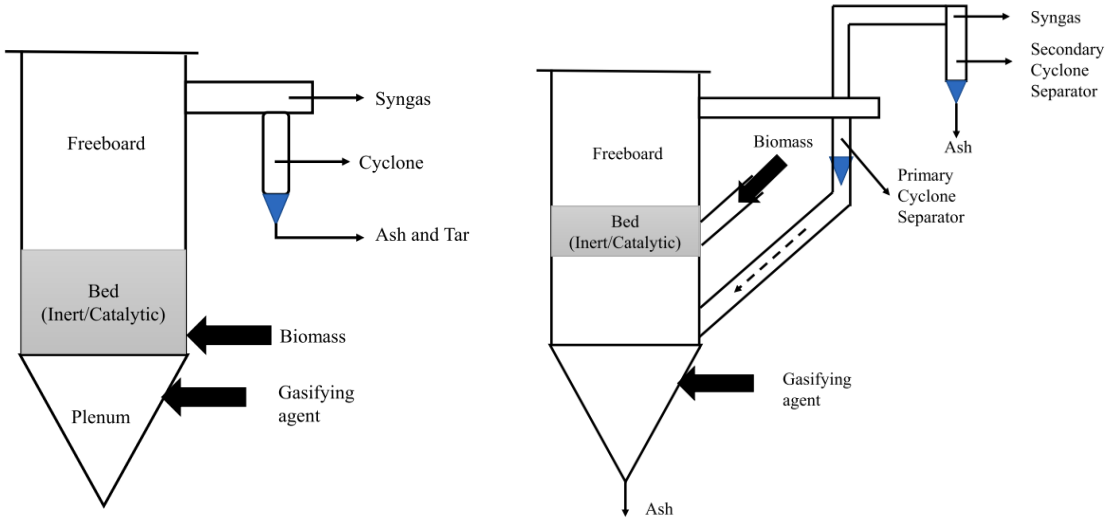

Figure 2.4: Schematic representation of (a) BFB and (b) CFB gasifiers. [18]

The different velocities of the gas stream in BFB gasifiers and CFB gasifiers result in a different structure of the reactors themselves. In BFB gasifiers, the gasifying agent enters at velocities typically lower than 1 m/s, allowing a fluidization process that keeps the form of a gas bubble mixture. This causes chemical reactions to take place to a greater extent in the dense bed region. Pneumatic transport of inert particles in the freeboard region is minimal, therefore a lower solid make-up is required. A cyclone is usually placed at the outlet of the gasifier to separate ash and tar from the gaseous stream [11, 18].

On the other hand, gas velocities reach values that usually range between 3 and 10 m/s in CFB gasifiers. These different operating conditions result

in a significant elutriation of the solid particles, which are dispersed along the entire height of the riser. This reactor configuration involves the use of a cyclone connected to a pipe to recirculate the particles transported by the gas. The product gas is then further sent to a filter capable of removing lighter solid particles such as ash and tars [11].

Focusing on the aim of this thesis, perhaps the most interesting potential of these types of gasifiers is the ability to operate at high pressures. The advantages of operating at pressurised conditions are manifold. First of all, the production of syngas at atmospheric conditions requires the installation of a downstream compressor, since most of the upgrading and reforming processes of the product gas from the gasifier are carried out at high pressures. The absence of this additional unit allows savings both in terms of operating expenses and capital expenditures [21]. In addition, having a pressurised gaseous product is also beneficial for all those processes that transform syngas into valuable chemicals, such as FT fuels and methanol [11]. However, it is important to be aware of how high pressures affect the hydrodynamics of fluidized bed gasifiers and how these operating conditions pose new challenges to overcome. In particular, under these conditions BFB gasifiers would require significant heights, while CFB gasifiers would have to be designed with such a narrow diameter that the supply of the solid phase would be very difficult [21].

For these reasons, Phoenix BioPower decided to design an hybrid fluidized bed (HFB) gasifier which, as the name suggests, represents a hybrid technology between BFB gasifiers and CFB gasifiers. This reactor configuration involves the use of inert particles of different diameters so that the heavier particles fluidize giving shape to a boiling bed, while the lighter particles are dragged by the gaseous current and recirculated thanks to a cyclone. Using this new technology, the conversion of biomass is accentuated and the size of the reactor is smaller compared to a BFB gasifier or a CFB gasifier of the same capacity. Furthermore, this gasification unit operates at lower gas velocities than a standard CFB reactor [21].

2.4 Bed material

As reported by Tezer et al.[17], the use of a bed material composed of inert particles is necessary in order to obtain a better fluidization of the solid phase. A higher fluidization quality results in better heat and mass transport and higher reaction efficiency.

Referring to Geldart's 1973 studies [22] can help understand which particles are best suited for this task. Powders are typically classified into 4

different groups according to their fluidization behaviour in ambient conditions using air.

The finest powders belong to group C of this classification and are characterised by a cohesive behaviour that makes it difficult to fluidize the bed. The tendency to agglomerate is due to the strong electrostatic forces exerted between particles, which counteract the drag force of the fluid entering the reactor. This leads to the formation of channels and discrete plugs along the bed height and makes it necessary to use mechanical stirrers to obtain a good mixing.

On the contrary, the most voluminous and dense particles fall into group D of this classification. In fluidized beds composed of this type of powders, a poor mixing of the solid phase, and a consequent consistent by-pass of the gas phase, can be observed. Large bubbles are formed at higher gas velocities and rise slowly through the bed particles leading to spouting. As reported by Kunii et al.[20], spoutable behaviour can also be problematic from a structural point of view as the walls of the gasifier can be seriously damaged.

An excellent fluidization quality is obtained by using group A and group B particles, defined respectively as aeratable and sand-like powders. Group A collects those powders characterised by a mean diameter from 45 to 150 μm and densities ranging between 800 and 1200 kg/m^3 [23]. The main characteristics of fluidized beds made up of these particles are a considerable expansion of the bed before reaching the bubble point and a slow collapse when the gaseous supply is suddenly interrupted. These properties are in contrast to the behaviour of group B particles, composed of powders with mean sizes between 150 and 1000 μm and densities that tend to range from 1.4 to 4 g/cm^3. These solid beds begin to expand once they almost reach the incipient bubbling condition and collapse rapidly when the gas stream is cut-off. Another notable difference concerns the appearance of bubbles as they rise up the bed. Bubbles size in aeratable particles is limited by a maximum threshold beyond which they become unstable and start dividing or not enlarging further. On the other hand, sand-like particles allow the formation of small bubbles at the bottom of the vessel that keep growing along the bed height.

According to Cocco et al. [23], larger bubbles are synonymous of lower mass transfers. Moreover, the higher gas velocity needed to suspend more voluminous solids means a lower gas residence time. Both these factors represent potential drawbacks for heterogeneous reactions compared to group A particles performances. However, remarkable disadvantages are related to the use of aeratable particles. Firstly, high pressure conditions can be translated into a lower density difference (ρ_p - ρ_f) between powders and fluid

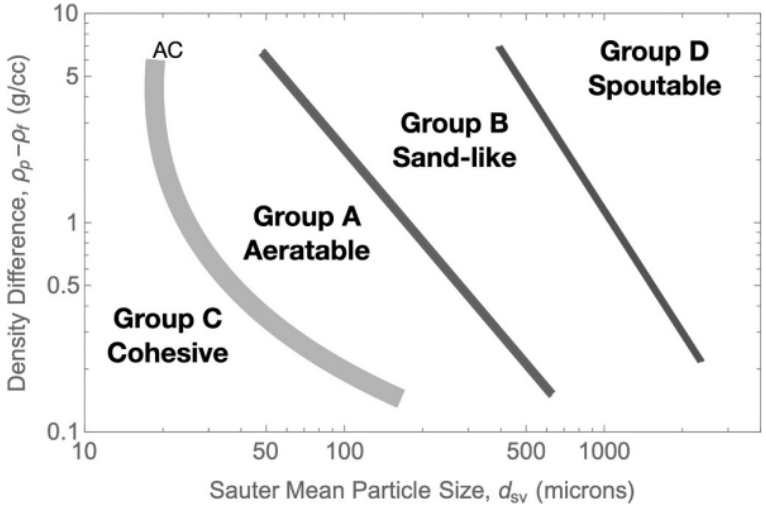

Figure 2.5: Geldart' classification of powders for fluidization by air at atmospheric conditions. [23]

phase. It is evident from Figure 2.5 that group A particles at high pressures can acquire fluid dynamics that are similar to those of group C particles. This factor can significantly affect the mixing quality inside the gasifier. In addition, it has been proved that irregularly shaped aeratable particles can actually behave as cohesive particles even under atmospheric conditions [24].

Natural group B particles are typically used for pyrolysis and gasification processes because of their thermal stability and their capability of offering a sufficiently high mixing. Both inert materials, like dolomite, silica, and limestone and catalytic materials can be used.

Silica sand is certainly one of the most used bed material and its attractiveness is due to its low cost, its availability and the absence of issues related to its disposal. However, problems associated to the agglomeration of ash components with the bed particles may occure during the gasification process [25].

Focusing on the catalytic options, as reported by Mishra et al. [18], several powders have been tested throughout the years with the aim of studying their effect on tar reduction, char conversion and product gas composition. Probably the most commonly used option is olivine, a naturally occurring iron-magnesium sand which has shown a catalytic effect on tar content reduction [25]. This bed material has been already employed in commercially active biomass gasification plants, like Güssing plant, located in Austria [26]. Beyond its low cost and its availability, it presents further advantages, like a

high attrition resistance [27]. Although the use of olivine is linked to some disadvantages, such as the difficult disposal of heavy metals contained in it and the catalytic activity related to undesired secondary reactions, this has not stopped researchers from studying and improving the performance of this mineral in the gasification process [25, 28].

In order to carry out the hydrodynamic studies of the gasifier, Phoenix BioPower decided to use silica sand as bed material. In addition, to simplify the CFD simulation, and since no reactions are examined for the purpose of this project, biomass pellets will not be taken into account and the solid phase will consist entirely of silica sand.

Chapter 3

Physical Background and Equations

3.1 Geometry

CFD analysis begins with the construction of the geometry of interest. The pilot-scale fluidized bed has been built using Design Modeler, available as an Ansys Fluent tool, and a 3D configuration has been chosen to better capture the characteristics of the air-sand flow.

The HFB gasifier, designed by Phoenix BioPower, consists of a cylindrical riser, a cyclone to separate the solid particles from the gas stream, and a standpipe to enable the solid circulation. A rectangular channel is used to connect the vertical riser to the cyclone, and a tangent inlet is shaped between the channel and the air-solid separator. Through a bubble cap distributor, the gas stream is injected into the solid bed. However, to simplify the CFD model, the presence of the distributor is not considered and the entire bottom section of the riser is assumed as a homogeneous gas inlet.

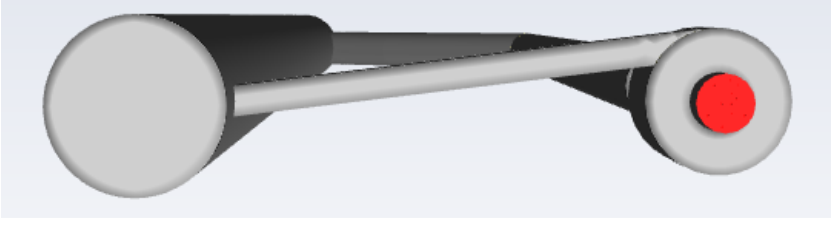

Figure 3.1: HFB gasifier - Top view.

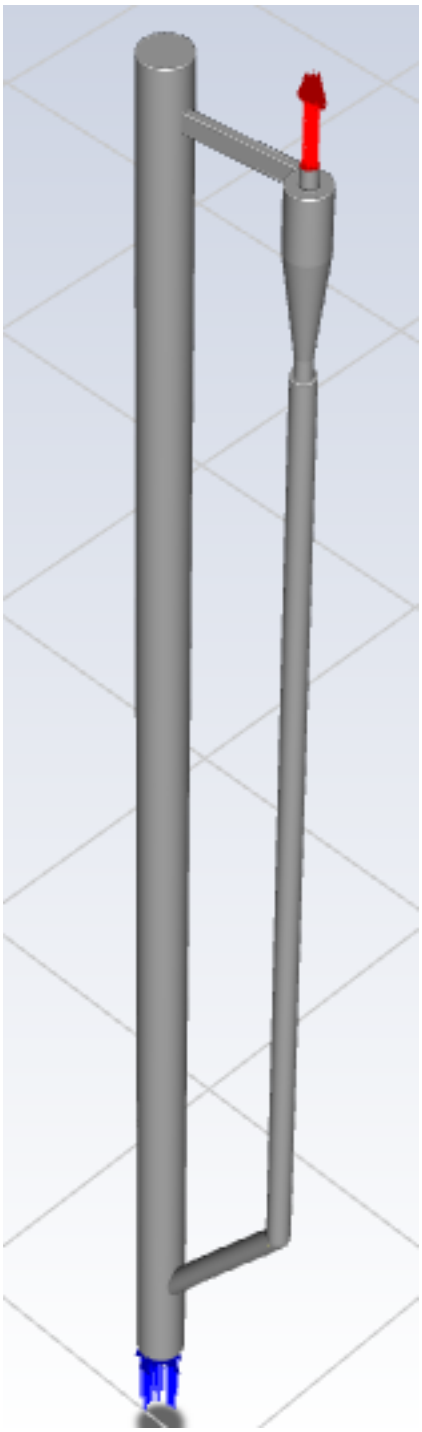

Figure 3.2: HFB gasifier - Isometric view.

Furthermore, the geometry is characterised by the presence of an orifice, placed near the intersection of the standpipe and the riser. The orifice is shaped as a metal surface perpendicular to the walls of the standpipe. This element will be neglected during the grid indipendence studies, exposed in Paragraph 5.1, to avoid overburdening the simulations in this initial step.

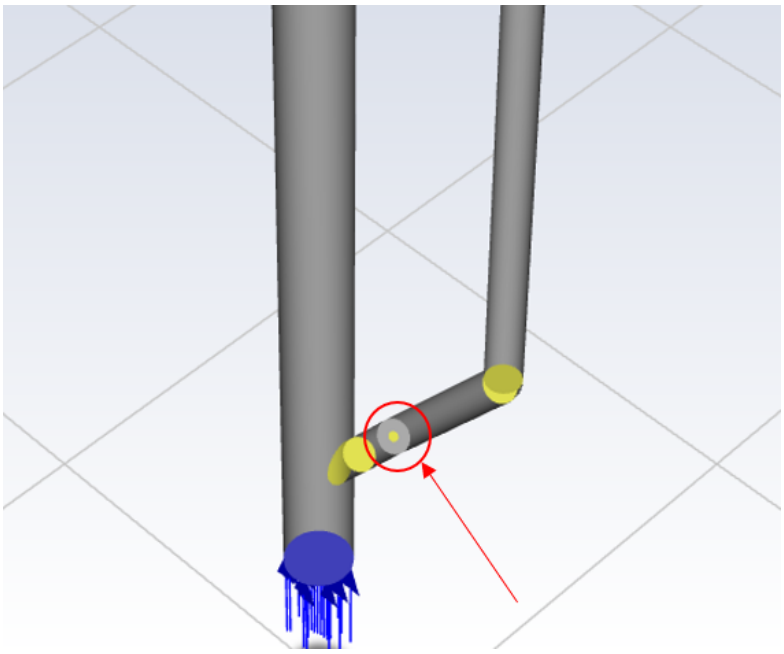

Figure 3.3: Detail of the HFB gasifier - Orifice.

3.2 System modeling

Fluid dynamics simulations are based on the assumption and resolution of physical models that best describe the system under consideration. Physical models consist of sets of equations that are solved iteratively and that are based on fundamental laws, such as the laws of conservation of momentum, energy and mass.

In this specific case, the hydrodynamic study of a biomass gasifier involves the simulation of the momentum transport of a multiphase flow, composed of a fluid phase and a solid phase. The solid particles represent the dispersed phase of the system, which is dissolved in a continuous gaseous phase. To model the dispersed-continuous phase interactions, it has been decided to adopt a full Eulerian model in which the two phases are treated as interpenetrating continua thanks to appropriate interaction terms. According

to Guan et al. [29], an Eulerian-Eulerian approach is suitable for all those commercial applications where parametric investigations and scale-up studies are performed. The Eulerian model theory is presented in the following paragraphs and refers to the Ansys Fluent Theory Guide [30].

3.2.1 Main model equations

The Eulerian model solves a set of n continuity and momentum equations, where n is the number of phases present in the system. For this reason, all these equations are multiplied by the volume fraction of the single phase. Continuity equations, also called mass conservation equations, of gas and solid particles respectively take the following form:

$$\frac{\partial}{\partial t}(\rho_g \alpha_g) + \nabla \cdot (\rho_g \alpha_g \mathbf{u_g}) = 0 \tag{3.1}$$

$$\frac{\partial}{\partial t}(\rho_s \alpha_s) + \nabla \cdot (\rho_s \alpha_s \mathbf{u_s}) = 0 \tag{3.2}$$

The term ρ refers to density and is measured in $[kg/m^3]$, while α represents the volume fraction of the considered phase $[-]$. Moreover, t is time $[s]$ and $\mathbf{u}$ is the velocity vector $[m/s]$, which can be decomposed into its components as reported:

$$\mathbf{u} = \begin{bmatrix} u_x \\ u_y \\ u_z \end{bmatrix} \tag{3.3}$$

Momentum equations, also known as Navier-Stokes equations, can be written as follows:

$$\frac{\partial}{\partial t}(\rho_g \alpha_g \mathbf{u_g}) + \nabla \cdot (\rho_g \alpha_g \mathbf{u_g} \mathbf{u_g}) = -\alpha_g \nabla p + \nabla \cdot \boldsymbol{\tau_g} + \rho_g \alpha_g \mathbf{g} - \beta(\mathbf{u_g} - \mathbf{u_s}) \tag{3.4}$$

$$\frac{\partial}{\partial t}(\rho_s \alpha_s \mathbf{u_s}) + \nabla \cdot (\rho_s \alpha_s \mathbf{u_s} \mathbf{u_s}) = -\alpha_s \nabla p + \nabla \cdot \boldsymbol{\tau_s} + \rho_s \alpha_s \mathbf{g} - \beta(\mathbf{u_s} - \mathbf{u_g}) - \nabla p_s \tag{3.5}$$

Looking at Equation (3.4) and Equation (3.5), it is possible to notice that the pressure p $[Pa]$, on the right hand side, does not have a subscript.

The cause of this formulation is that the pressure field is shared between the solid and the gas phase. The term **g** refers to the acceleration due to gravity and, according to the coordinate system adopted for the geometry, it can be defined as follows:

$$\mathbf{g} = \begin{bmatrix} 0 \\ -9.81 \\ 0 \end{bmatrix} \frac{m}{s^2} \tag{3.6}$$

$\boldsymbol{\tau_g}$ and $\boldsymbol{\tau_s}$ represent the stress-strain tensors of the gas and the solid phase $[kg/(m * s^2)]$, which can be formulated in the following way:

$$\boldsymbol{\tau_g} = -\alpha_g \mu_g [\nabla \mathbf{u_g} + (\nabla \mathbf{u_g})^T] - \frac{2}{3} \alpha_g \mu_g \nabla \cdot \mathbf{u_g} \mathbf{I} \tag{3.7}$$

$$\boldsymbol{\tau_s} = -\alpha_s \mu_s [\nabla \mathbf{u_s} + (\nabla \mathbf{u_s})^T] - \alpha_s (\lambda_s - \frac{2}{3} \mu_s) \nabla \cdot \mathbf{u_s} \mathbf{I} \tag{3.8}$$

$\boldsymbol{\tau_g}$ depends not only on the volume fraction of gas and the gas velocity, but also on the gas viscosity μ_g $[kg/(m * s)]$. On the other hand, $\boldsymbol{\tau_s}$ is expressed as a function of the granular viscosity μ_s $[kg/(m * s)]$ and the granular bulk viscosity λ_s $[kg/(m*s)]$. These and other properties, including solid pressure p_s $[Pa]$, already mentioned in Equation (3.5), are defined in accordance with the kinetic theory of granular flows, exposed in detail in Paragraph 3.2.3.

Finally, the source term $\beta(\mathbf{u}_g$ - $\mathbf{u}_s)$, which appears in both the momentum equations (3.4) and (3.5), represents the momentum transfer between the gas phase and the solid particles. The momentum transfer coefficient β $[kg/(m^3 * s)]$ can be shaped in several ways depending on the drag force model chosen by the user.

3.2.2 Drag force model

As already discussed, the velocity field of the particles and the velocity field of the gas phase are calculated separately in each individual unit volume of the geometry. The difference between these two velocities is due to interphase transfer forces. In particular, the interphase drag force turns out to be the predominant momentum transfer mechanism. The general form of the drag force per unit volume acting between the primary phase and the secondary phase is

$$D_{sg} = \frac{1}{2} \rho_g C_D \frac{A_P}{V} (\mathbf{u_s} - \mathbf{u_g}) |\mathbf{u_s} - \mathbf{u_g}| \tag{3.9}$$

where A_p/V is the interfacial area per unit volume $[1/m]$ and C_D is the drag coefficient $[-]$. These two properties are left up to the user and are the properties that govern the interphase drag force. According to Guan et al. [29], the drag model chosen by the user has a relevant effect on the flow behaviour. Drag models proposed by Gidaspow [31], Syamlal & O'Brien [32] and Yang et al. [33] are three commonly used models which are in good agreement with experiments carried out with bubbling beds. However, the former two models allow a better prediction of the flow behaviour in the riser.

Gidaspow's model has been widely used to describe the fluid dynamics of numerous BFB and CFB reactors built for different applications, including biomass gasification [29, 34–40]. For this reason, this drag model has been chosen to describe the momentum transfer mechanism between the particles and the gas phase considered in the current study.

Gidaspow described the interphase momentum transfer coefficient β combining the Ergun equation [41] and the Wen-Yu model [42]. When the volume fraction of gas α_g is lower than or equal to 0.8, β assumes the following form:

$$\beta_{Ergun} = 150\frac{(1-\alpha_g)^2\mu_g}{\alpha_g {d_s}^2} + 1.75\frac{(1-\alpha_g)\rho_g|\mathbf{u_g}-\mathbf{u_s}|}{d_s} \tag{3.10}$$

where d_s is the diameter of the solid particles $[m]$.
When α_g is higher than 0.8, β can be written as follows:

$$\beta_{Wen-Yu} = \frac{3}{4}\frac{(1-\alpha_g)\alpha_g\rho_g|\mathbf{u_g}-\mathbf{u_s}|}{d_s} C_D {\alpha_g}^{-2.65} \tag{3.11}$$

The drag coefficient C_D is defined as follows:

$$C_D = \begin{cases} \frac{24}{Re_s}[1+0.15Re_s^{0.687}], & Re_s \leq 1000 \\ 0.44, & Re_s > 1000 \end{cases} \tag{3.12}$$

where the particle Reynolds number Re_s $[-]$ assumes the following form:

$$Re_s = \frac{\alpha_g\rho_g d_s|\mathbf{u_g}-\mathbf{u_s}|}{\mu_g} \tag{3.13}$$

3.2.3 Kinetic theory of granular flows

In order to formulate the momentum transport equation of the solid phase (3.5) in the canonical form, properties typically associated with the description

of fluids, such as viscosity and pressure, have been incorporated. To deal with these properties, Ansys Fluent uses the kinetic theory of granular flows (KTGF), which represents a valid closure law to describe the rheology of the solid particles.

KTGF is an attempt to model granular flows doing an analogy between the motion of suspended particles and the chaotic motion of gas molecules [43]. According to the kinetic theory of gases, the thermodynamic temperature of a gaseous fluid (T) is closely related to the mean kinetic energy of the gas molecules ($\overline{K}$):

$$\overline{K} = \frac{3}{2} k_B T \tag{3.14}$$

where

$$k_B = 1.83 * 10^{-23} [\frac{J}{K}] \tag{3.15}$$

Solid particles in fluidized beds are characterized by a certain velocity, which can be seen as the sum of the mean velocity of the bulk material and a fluctuation component:

$$\mathbf{u_s} = \overline{\mathbf{u_s}} + \mathbf{u_s}' \tag{3.16}$$

Analogous to the thermodynamic temperature for a gas, it is possible to define a granular temperature as the mean kinetic energy of the particle velocity fluctuations $[m^2/s^2]$:

$$\Theta = \frac{1}{3} \langle u_{s,i} u_{s,i} \rangle \tag{3.17}$$

where $u_{s,i}$ is the i^{th} component of the fluctuating particles velocity in the Cartesian coordinate system and $\langle\ \rangle$ represents the ensemble average.

Starting from this definition, Ding et al. [44] derived a granular temperature transport equation which takes the following form:

$$\frac{3}{2} \left[\frac{\partial}{\partial t} (\rho_s \alpha_s \Theta) + \nabla \cdot (\rho_s \alpha_s \mathbf{u_s} \Theta) \right] = (-p_s \mathbf{I} + \boldsymbol{\tau_s}) : \nabla \mathbf{u_s} + \nabla \cdot (k_\Theta \nabla \Theta) - \gamma_s - \phi_{sg} \tag{3.18}$$

where

- $(-p_s\mathbf{I} + \boldsymbol{\tau_s}) : \nabla \mathbf{u}_s$ is the generation term linked to the solids stress tensor,
- $(k_\Theta \nabla \Theta)$ represents the diffusion of energy,
- γ_s is the collisional dissipation of energy,
- ϕ_{sg} is the energy exchanged between the gaseous phase and the solid particles.

Among all the available options, Equation (3.18) is solved through the algebraic formulation, which neglects the influence of both the convective and the diffusive term.

The first generation term listed above contains the solids pressure p_s, defined as the normal force due to particles interaction. Solids pressure is calculated when the volume fraction of solids is lower than the maximum packing limit, and is used to derive the pressure gradient term which appears in the momentum transport equation of the solid phase (3.5). An expression of this property is provided by Lun et al. [45] who wrote the solids pressure as the sum of a kinetic term and a second term linked to particle collisions:

$$p_s = \alpha_s \rho_s \Theta + 2\rho_s(1 + e_{ss})\alpha_s^2 g_{0,ss}\Theta \tag{3.19}$$

e_{ss} is the coefficient of restitution for particle collisions $[-]$ which can be adjusted by the user depending on the particle features. Upadhyay et al. [34] proved that particle-particle restitution coefficients ranging between 0.8 and 0.9 offer a good prediction of hydrodynamic studies of CFB risers. For this reason, a restitution coefficient equal to 0.9 has been set to study the behaviour of silica sand.

The radial distribution function $g_{0,ss}$ is a correction term which influences the probability of collisions between particle when the packing density becomes higher. It can be defined as a non-dimensional distance between solid spheres:

$$g_{0,ss} = \frac{s + d_s}{s} \tag{3.20}$$

where s is the distance between the particles $[m]$. When the volume fraction of the solid phase is close to the maximum packing limit, the distance between the grains becomes negligible ($s \to 0$), therefore $g_{0,ss} \to \infty$. A high value of the radial distribution function accentuates the effect of particle

collisions in the definition of the solids pressure. On the other hand, a higher spacing between solid particles can be translated into a lower influence of the distribution function ($g_{0,ss} \rightarrow 1$). This condition allows the kinetic term to get a major role in solids pressure generation.

An empirical formulation of the radial distribution factor is used by Ansys Fluent when a single solid phase is present in the system [31]:

$$g_{0,ss} = \left[1 - \left(\frac{\alpha_s}{\alpha_{s,Max}} \right)^{\frac{1}{3}} \right]^{-1} \tag{3.21}$$

where $\alpha_{s,Max}$ is the maximum packing limit [−]. This value is not fixed, but it can vary depending on the particle size and shape. Kunii et al. [20] proposed an empirical correlation between the bed voidage ϵ_m and the sphericity Φ_s of the solid grains.

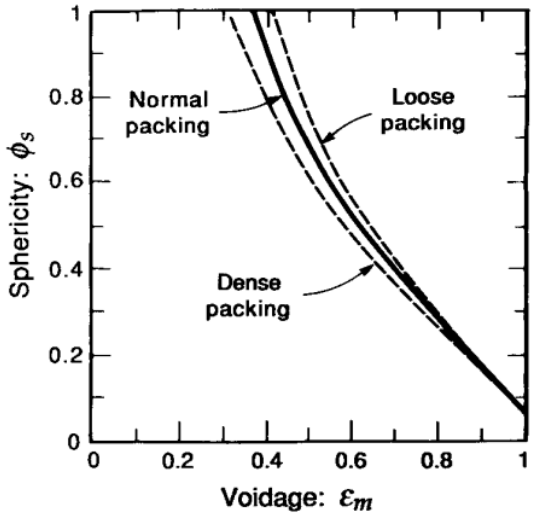

Figure 3.4: Voidage of a randomly packed bed as a function of the shape factor of uniformly sized particles. [20]

According to Rorato et al. [46] and Pecate et al. [47], sand particles used for engineering applications are characterised by a sphericity that can be approximated by the value 0.85. Looking at Fig 3.4, a sphericity equal to 0.85 corresponds to a bed voidage ranging between 0.3 and 0.4 in dense packing conditions. Therefore, a maximum packing limit equal to 0.63, proposed by Ansys Fluent as default value, has been kept for this CFD simulation.

Keeping the focus on the first generation term of the granular temperature, present in Equation (3.18), the stress tensor $\boldsymbol{\tau_s}$ is examined in more

depth. From Equation (3.8), it is possible to notice that the solids stress tensor depends on both shear viscosity μ_s and bulk viscosity λ_s due to particles momentum exchange because of collisions and translation.

The solids bulk viscosity describes the resistance of the sand particles to expansion and compression phenomena and is modeled in accordance with Lun et al. [45]:

$$\lambda_s = \frac{4}{3}\alpha_s^2 \rho_s d_s g_{0,ss}(1+e_{ss}) \left(\frac{\Theta}{\pi}\right)^{\frac{1}{2}} \tag{3.22}$$

The shear viscosity can be decomposed into the sum of a collisional, a kinetic and a frictional part. The latter component is included to shape the viscous-plastic transition when the solids volume fraction reaches the packing limit.

$$\mu_s = \mu_{s,col} + \mu_{s,kin} + \mu_{s,fr} \tag{3.23}$$

The collisional viscosity can be written as follows [48]:

$$\mu_{s,col} = \frac{4}{5}\alpha_s \rho_s d_s g_{0,ss}(1+e_{ss}) \left(\frac{\Theta}{\pi}\right)^{\frac{1}{2}} \tag{3.24}$$

Different options are available to model the kinetic part of the shear viscosity. As reported by Upadhyay et al. [34], Syamlal et al. [49] granular viscosity offers a reliable prediction of particles behaviour in the middle and in the higher region of the riser, but it overpredicts the solid holdup in the lower section. On the contrary, Gidaspow et al. [48] model shows the best agreement with the experimental results for the lower region of the riser and overpredicts the solids volume fraction in the top and mid-section. However, both the viscosity models give a satisfactory description of the hydrodynamics of silica sand. Therefore, the current study uses Gidaspow et al. [48] viscosity, which can be defined in the following way:

$$\mu_{s,kin} = \frac{10\rho_s d_s \sqrt{\Theta\pi}}{96\alpha_s g_{0,ss}(1+e_{ss})} \left[1 + \frac{4}{5}\alpha_s g_{0,ss}(1+e_{ss})\right]^2 \tag{3.25}$$

The frictional component of the shear viscosity play an important role in dense flows at low shear, where friction between grains is the main cause of

stress. This component is described by Schaeffer [50] through the following equation:

$$\mu_{s,fr} = \frac{p_{friction} sin\phi}{2\sqrt{I_{2D}}} \tag{3.26}$$

where $p_{friction}$ is the frictional pressure $[Pa]$, ϕ represents the angle of internal friction $[deg]$ and I_{2D} is the second invariant of the deviatoric stress tensor $[1/s^2]$.

In dense granular flows, the KTGF does not offer an accurate description of the silica sand hydrodynamics, as instantaneous collisions are no longer relevant compared to the frictional stresses due to the contacts between solid particles. Ansys Fluent allows the user to set a frictional packing limit, beyond which the frictional stress is summed to the shear stress predicted by the kinetic theory. Considering the frictional component, the solids pressure and the shear viscosity can be reformulated in the following way:

$$p_s = p_{kinetic} + p_{friction} \tag{3.27}$$

$$\mu_s = \mu_{s,kin} + \mu_{s,fr} \tag{3.28}$$

The frictional pressure can be easily solved using the ktgf-based model. According to this option, the calculation of the frictional viscosity uses directly the solids pressure obtained through Equation (3.19), where the high density of particles is taken into account by the radial distribution function. Furthermore, as Wei et al. [38] also did for their CFD study, an angle of internal friction of 30° has been set. The frictional packing limit has been kept equal to 0.61, default value provided by Ansys Fluent.

Shifting the focus on the second generation term mentioned in Equation (3.18), i.e., the diffusive flux of granular energy, the following expression can be written for the diffusion coefficient k_Θ:

$$k_\Theta = \frac{150\rho_s d_s\sqrt{\Theta\pi}}{384 g_{0,ss}(1+e_{ss})}\left[1+\frac{6}{5}\alpha_s g_{0,ss}(1+e_{ss})\right]^2 + 2\rho_s\alpha_s^2 g_{0,ss}(1+e_{ss})\sqrt{\frac{\Theta}{\pi}} \tag{3.29}$$

Moving to the third generation term, which represents the loss of energy due to particle collisions, the expression provided by Lun et al. [45] can be used:

$$\gamma_\Theta = \frac{12(1-e_{ss}^2)g_{0,ss}}{d_s\sqrt{\pi}}\rho_s\alpha_s\Theta^{\frac{3}{2}} \tag{3.30}$$

Finally, the energy exchanged between the solid phase and the gas phase because of particle velocity fluctuations, can be expressed as follows [48]:

$$\phi_{sg} = -3\beta\Theta \tag{3.31}$$

To summarise the main model settings described in these paragraphs, a list of the variables defined by the user are comprehensively reported in the following table.

Table 3.1: Eulerian model settings used in the simulation.

Phase Interaction	
Drag coefficient (Gas - Solid Interactions)	Gidaspow
Restitution coefficient e_{ss} (Solid - Solid Interactions)	0.9
Granular properties	
Granular viscosity ($\mu_{s,kin}$)	Gidaspow
Granular bulk viscosity (λ_s)	Lun et al.
Solids pressure (p_s)	Lun et al.
Granular temperature (Θ)	algebraic
Frictional viscosity ($\mu_{s,fr}$)	Schaeffer
Frictional pressure ($p_{friction}$)	ktgf-model
Friction packing limit	0.61
Angle of internal friction (Φ)	30.00007
Packing limit ($\alpha_{s,Max}$)	0.63
Radial distribution ($g_{0,ss}$)	Lun et al.

3.2.4 Turbulence model

Numerous engineering applications, including the hydrodynamic studies of interest, are conducted in turbulent conditions. It is well known that, in case of turbulent flows, small variations in the fluids velocities generate instabilities within the system, which result in the presence of vortices and an overall chaotic and unpredictable motion.

The most popular way to model these instabilities is using the Reynolds decomposition approach, which decomposes the instantaneous velocity of fluids into the sum of an average bulk velocity and a velocity fluctuation.

$$\mathbf{u} = \overline{\mathbf{u}} + \mathbf{u}' \tag{3.32}$$

Considering the specific case of an airflow inside the gasifier, and temporarily neglecting the presence of the solid fraction, the continuity equation and the momentum transport equation of the gas phase must be rewritten in the following way:

$$\frac{\partial}{\partial t}(\rho_g) + \nabla \cdot [\rho_g(\overline{\mathbf{u_g}} + \mathbf{u_g}')] = 0 \tag{3.33}$$

$$\frac{\partial}{\partial t}[\rho_g(\overline{\mathbf{u_g}} + \mathbf{u_g}')] + \nabla \cdot [\rho_g(\overline{\mathbf{u_g}} + \mathbf{u_g}')(\overline{\mathbf{u_g}} + \mathbf{u_g}')] = -\nabla(\overline{p} + p') + \nabla \cdot \boldsymbol{\tau_g} + \rho_g \mathbf{g} \tag{3.34}$$

where

$$\boldsymbol{\tau_g} = -\mu_g[\nabla(\overline{\mathbf{u_g}} + \mathbf{u_g}') + (\nabla(\overline{\mathbf{u_g}} + \mathbf{u_g}'))^T] - \frac{2}{3}\mu_g \nabla \cdot (\overline{\mathbf{u_g}} + \mathbf{u_g}')\mathbf{I} \tag{3.35}$$

Applying the Reynolds mean of all the terms present in the conservation laws, Equations (3.33) and (3.34) can be formulated as follows:

$$\frac{\partial}{\partial t}(\rho_g) + \nabla \cdot \rho_g \overline{\mathbf{u_g}} = 0 \tag{3.36}$$

$$\frac{\partial}{\partial t}\rho_g \overline{\mathbf{u_g}} + \nabla \cdot (\rho_g \overline{\mathbf{u_g}}\,\overline{\mathbf{u_g}}) + \nabla \cdot (\rho_g \overline{\mathbf{u_g}'\mathbf{u_g}'}) = -\nabla \overline{p} + \nabla \cdot \boldsymbol{\tau_g} + \rho_g \mathbf{g} \tag{3.37}$$

where

$$\boldsymbol{\tau_g} = -\mu_g[\nabla\,\overline{\mathbf{u_g}} + (\nabla\,\overline{\mathbf{u_g}})^T] - \frac{2}{3}\mu_g \nabla \cdot \overline{\mathbf{u_g}}\,\mathbf{I} \tag{3.38}$$

The expression $\rho_g \overline{\mathbf{u}_g' \mathbf{u}_g'}$ is called Reynolds turbulent stress tensor and it represents the fluid capability of transporting momentum thanks to the turbulent velocity fluctuations.

$$\boldsymbol{\tau_g^t} = \rho_g \overline{\mathbf{u_g}' \mathbf{u_g}'} \tag{3.39}$$

Equation (3.39) can be arranged in the following way:

$$\boldsymbol{\tau_g^{(t)}} = -\boldsymbol{\Sigma_g^{(t)}} = (-\rho_g \overline{\mathbf{u_g}' \mathbf{u_g}'} + \frac{2}{3}\rho_g k \mathbf{I}) - \frac{2}{3}\rho_g k \mathbf{I} \tag{3.40}$$

where k represents the turbulent kinetic energy per unit mass $[m^2/s^2]$ and is obtained by adding all the elements on the diagonal of the Reynolds stress tensor and multiplying the sum by 0.5.

$$k = \frac{1}{2}(\overline{u_x' u_x'} + \overline{u_y' u_y'} + \overline{u_z' u_z'}) \tag{3.41}$$

According to Equation (3.40), $\boldsymbol{\tau_g^{(t)}}$ is decomposed into a normal stress tensor, which can be combined with the pressure term present in the momentum equation

$$\overline{P} = \overline{p} - \frac{2}{3}\rho_g k \mathbf{I} \tag{3.42}$$

and a deviatoric stress tensor, given by

$$\mathbf{D^{(t)}} = -(\rho_g \overline{\mathbf{u_g}' \mathbf{u_g}'} - \frac{2}{3}\rho_g k \mathbf{I}) \tag{3.43}$$

The deviatoric stress tensor depends on the fluid velocity fluctuations which, not being directly calculable, require a different formulation, in order to successfully model the turbulent flow. In fluid dynamics, Boussinesq approximation is commonly used to rewrite $\mathbf{D}^{(t)}$ with an expression analogous to Newton's constitutive law for the shear stress tensor.

$$\mathbf{D^{(t)}} = -\mu_g^{(t)} \left[\nabla \overline{\mathbf{u_g}} + (\nabla \overline{\mathbf{u_g}})^T - \frac{2}{3} \nabla \cdot \overline{\mathbf{u_g}}\, \mathbf{I} \right] \tag{3.44}$$

Introducing the turbulent viscosity $\mu_g^{(t)}$ $[kg/(m*s)]$, the momentum transport equation can be finally written as follows:

$$\frac{\partial}{\partial t}\rho_g\overline{\mathbf{u_g}} + \nabla\cdot(\rho_g\overline{\mathbf{u_g}}\,\overline{\mathbf{u_g}}) = -\nabla\overline{P} + \rho_g\mathbf{g} + \nabla\cdot\Big\{-(\mu_g+\mu_g^{(t)})\left[\nabla\,\overline{\mathbf{u_g}} + (\nabla\,\overline{\mathbf{u_g}})^T - \frac{2}{3}\mu_g\nabla\cdot\overline{\mathbf{u_g}}\,\mathbf{I}\right]\Big\} \tag{3.45}$$

All turbulent models built on the Reynolds-averaged continuity and momentum transport equations are called RANS (Reynolds-averaged Navier-Stokes) models. These models differ from each other based on the number and type of additional equations solved to close the fluctuating properties present in the system, such as $\mu_g^{(t)}$.

In the current CFD study, turbulence is assessed through the realizable k-ϵ model, to capture the complex hydrodynamics of the airflow. Starting from the solution of the continuous phase, the behaviour of the multiphase air-sand system is determined by the dispersed turbulence method.

Realizable k-ϵ model

Although turbulent viscosity is coupled to the molecular viscosity in Equation (4.7), this property is not an intrinsic characteristic of the fluid, but it is introduced to predict the stress caused by velocity fluctuations when the flow is turbulent. The realizable k-ϵ model assumes turbulent viscosity as a function of the turbulent kinetic energy k $[m^2/s^2]$ and its dissipation rate ϵ $[m^2/s^3]$

$$\mu^{(t)} = -\rho C_\mu \frac{k^2}{\epsilon} \tag{3.46}$$

where C_μ is a constant and is equal to 0.09.

Therefore, this turbulence model requires the resolution of two more transport equations, in addition to the Reynolds-averaged mass and momentum conservation laws. The k transport equation is given by

$$\frac{\partial}{\partial t}(\rho k) + \nabla\cdot(\rho k\mathbf{u}) = \nabla\cdot\left[\left(\mu + \frac{\mu^{(t)}}{\sigma_k}\right)\nabla k\right] + G_k + G_b - \rho\epsilon - Y_M \tag{3.47}$$

where G_k and G_b represent the generation terms due to the mean velocity gradients and buoyancy respectively, Y_M considers the effect of fluctuating dilatation on the overall dissipation rate, while σ_k is a turbulent Prandtl number which assumes a constant value.

The dissipation rate transport equation assumes the following form:

$$\frac{\partial}{\partial t}(\rho\epsilon) + \nabla \cdot (\rho\epsilon\mathbf{u}) = \nabla \cdot \left[\left(\mu + \frac{\mu^{(t)}}{\sigma_\epsilon}\right)\nabla\epsilon\right] + \rho C_1 S\epsilon - \rho C_2 \frac{\epsilon^2}{k + \sqrt{\nu\epsilon}} + C_{1\epsilon}\frac{\epsilon}{k} C_{3\epsilon} G_b \tag{3.48}$$

where ν is the kinematic viscosity of the fluid, σ_ϵ is a second turbulent Prandtl number and C_1, C_2, $C_{1\epsilon}$ and $C_{3\epsilon}$ are constants. In particular,

$$C_1 = max\left[0.43, \frac{\eta}{\eta + 5}\right], \ \ \eta = S\frac{k}{\epsilon} \tag{3.49}$$

Finally, S represents the modulus of the mean rate-of-strain tensor and is expressed as follows:

$$S = \sqrt{2S_{ij}S_{ij}} \tag{3.50}$$

What distinguishes this k-ϵ model from RNG and standard k-ϵ model is the "realizability". To understand the meaning of this term, it is necessary to start from the definition of normal Reynolds stress which, for an incompressible fluid, can be written as

$$\overline{u^2} = \frac{2}{3}k + 2\nu^{(t)}\frac{\partial U}{\partial x} \tag{3.51}$$

$\overline{u^2}$ is by definition a positive quantity. However, this term becomes negative ("non-realizable") when the strain is sufficiently large to satisfy

$$\frac{k}{\epsilon}\frac{\partial U}{\partial x} > \frac{1}{3C_\mu} \approx 3.7 \tag{3.52}$$

Moreover, a large mean strain rate can violate the Schwarz inequality for shear stresses, defined as $((\overline{u_\alpha}\,\overline{u_\beta})^2 \leq \overline{u_\alpha^2 u_\beta^2})$. To ensure the positivity of $\overline{u^2}$ and Schwarz inequality, C_μ is not assumed as a fixed value, but is expressed as a function of k, ϵ, and the mean strain and rotation rates.

Dispersed method

In order to model the biphasic system of interest, the realizable k-ϵ model is integrated with a method capable of describing the behaviour of both solid and gaseous phase. Since a primary continuous phase and a secondary dispersed phase are clearly recognizable within the system, the dispersed method has been chosen for the CFD simulation.

Continuous phase motion is predicted using the k-ϵ model equations, supplemented with extra terms which refer to the interphase turbulent momentum transfer. Additionally, a phase-weighted averaging process is employed to avoid volume fraction fluctuations into the continuity equations.

The Reynolds stress tensor for the gas phase can be written as follows:

$$\boldsymbol{\tau}_{\boldsymbol{g}}^{(t)} = -\frac{2}{3}(\rho_g k_g + \rho_g \nu_g^{(t)} \nabla \cdot \mathbf{U_g})\mathbf{I} + \rho_g \nu_g^{(t)}(\nabla \mathbf{U_g} + \nabla \mathbf{U_g}^T) \tag{3.53}$$

where $\mathbf{U}_q$ is the phase-weighted velocity.

The modified k and ϵ transport equations take the following form:

$$\frac{\partial}{\partial t}(\alpha_g \rho_g k_g) + \nabla \cdot (\alpha_g \rho_g k_g \mathbf{U_g}) = \nabla \cdot \left[\alpha_g \left(\mu_g + \frac{\mu_g^{(t)}}{\sigma_k}\right) \nabla k_g\right] + \alpha_g G_{k,g} \\ -\alpha_g \rho_g \epsilon_g + \alpha_g \rho_g \Pi_{k_g} \tag{3.54}$$

$$\frac{\partial}{\partial t}(\alpha_g \rho_g \epsilon_g) + \nabla \cdot (\alpha_g \rho_g \epsilon_g \mathbf{U_g}) = \nabla \cdot \left[\alpha_g \left(\mu_g + \frac{\mu_g^{(t)}}{\sigma_\epsilon}\right) \nabla \epsilon_g\right] \\ +\alpha_g \frac{k_g}{\epsilon_g}(C_{1\epsilon} G_{k,g} - C_{2\epsilon} \rho_g \epsilon_g) + \alpha_g \rho_g \Pi_{\epsilon_g} \tag{3.55}$$

where the source terms containing Π_{k_g} and Π_{ϵ_g} are terms which can be added to consider the influence of the dispersed phase on the continuous phase.

On the other hand, turbulent predictions of the dispersed phase are not obtained through the resolution of transport equations, but correlation functions, dispersion coefficients and turbulent kinetic energy of the sand particles are calculated from time and length scales of the motion.

All the settings of the realizable $k-\epsilon$ dispersed model are summarised in the following table.

Table 3.2: Turbulence model settings.

Model	
$k-\epsilon$ (2 Equations)	
k- ϵ Model	
Realizable	
Turbulence multiphase model	
Dispersed	
Model constants	
$C_{2\epsilon}$	1.9
$C_{3\epsilon}$	1.3
σ_k (TKE Prandtl number)	1
σ_ϵ (TDR Prandtl number)	1.2
σ_{pq} (Dispersion Prandtl number)	0.75

Chapter 4

Numerical Methods

Validation and understanding of a physical system require the ability to apply the desired set of equations to a domain of interest. However, the numerical solution of these mathematical models requires two different levels of discretization. Firstly, the continuous exact solutions provided by partial differential equations must be replaced by discrete values, which are computed by solving a set of algebraic equations. Moreover, the construction of a computational grid is needed to predict the distribution of the property of interest over the whole geometric domain.

In this chapter, the different steps of the discretization process is examined, from the new formulation of both physical domain and physical phenomenon to the solution of the resulting algebraic equations. The discussion about the mathematical aspects refers to the notions presented by Moukalled et al. in *The Finite Volume Method in Computational Fluid Dynamics - An Advanced Introduction with OpenFOAM® and Matlab®* [51].

4.1 Domain discretization

The discretization of the physical domain results in the subdivision of the gasifier volume into a finite number of non-overlapping cells, able to completely fill the original geometry. All these discrete elements are defined by a set of vertices and bounded by faces, which are typically shared with neighboring elements, except at the boundaries.

Different meshing techniques may be used to discretized the computational domain. A first distinction is done between structured grids and unstructured grids.

In a 3D geometry, a structured grid consists of hexahedral cells (elements with six faces) which allow a straightforward indexing and identification of

neighboring cells. On the other hand, unstructured grids are built from elements of different shapes, like pyramids, prisms and tetrahedra. Structured mesh are preferred because they require less memory and because of their better numerical properties [52].

As confirmed by Tu et al. [53], a common structured mesh which is widely used for circular cylinders is the O-grid mesh. This type of mesh has been employed to discretize all the cylindrical parts of the HFB gasifier, including the area close to the orifice, albeit with a finer discretization. The "Fluent Meshing" tool has been used for the purpose.

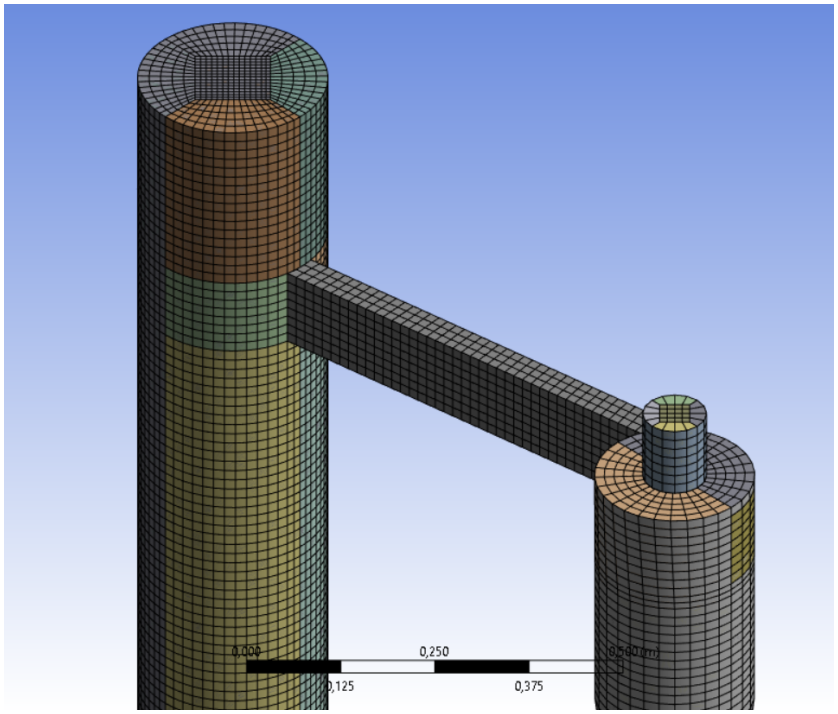

(a) Isometric view

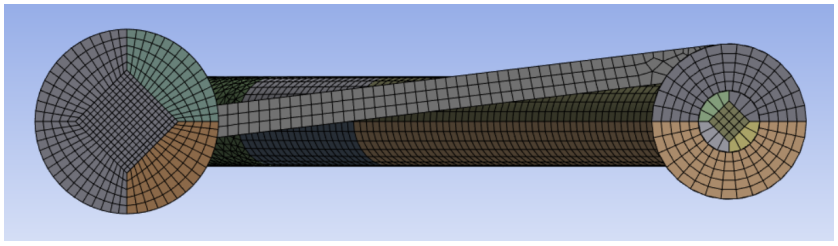

(b) Top view

Figure 4.1: Result of the meshing process.

However, it was not possible to model the entire geometry with a structured mesh, because of the sharp angle present at the elbow of the standpipe and the junction between the riser and the standpipe. The solver can handle both structured and unstructured grids, and for these two portions of the geometry, tetrahedral and pyramidal cells have been used to complete the discretization of the domain.

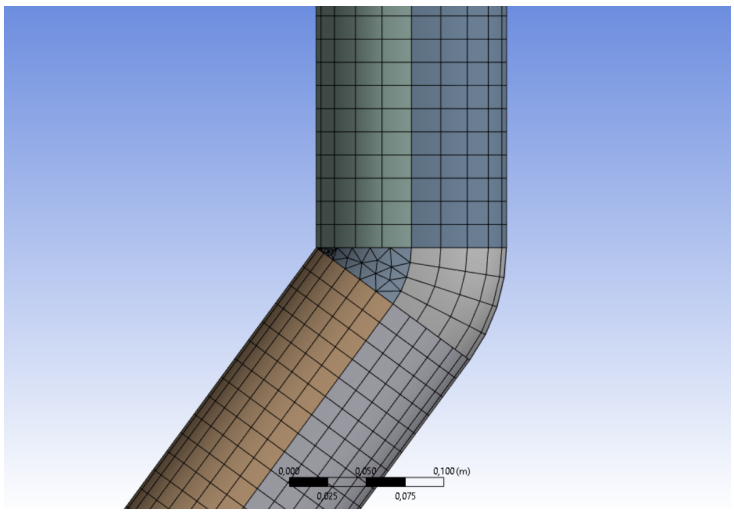

(a) Elbow

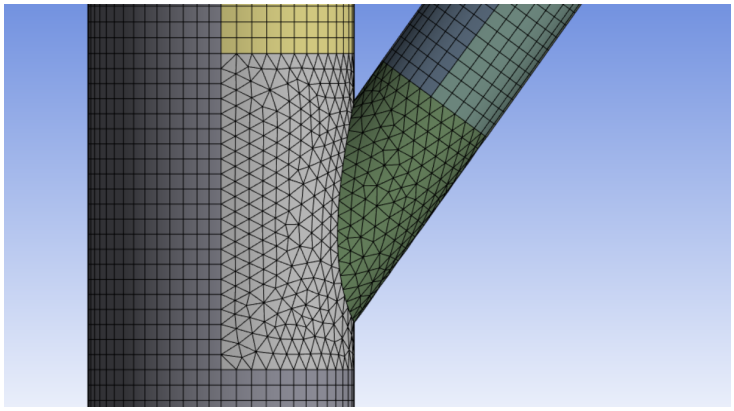

(b) Junction riser-standpipe

Figure 4.2: Portions with unstructured mesh.

Regardless of the type of mesh, the computational grid must always meet certain quality parameters which assure the accuracy and stability of the CFD simulations. The distribution of node points, smoothness, and skewness are some of the cell properties which are typically used to asses the mesh

quality. The evaluation of quality criteria varies depending on the cell types present in the mesh, whether they are tetrahedral, hexahedral, polyhedral, and so forth [54].

The computational grid employed to discretize the geometry of the HFB gasifier is evaluated by Ansys Fluent through four different parameters:

- *Aspect ratio.* The aspect ratio serves as a metric for the elongation of a cell, calculated by determining the ratio of the maximum value to the minimum value among certain distances between the cell centroid and face centroids, as well as the distances between the cell centroid and nodes [54]. This value should be kept below 5 [52].

- *Skewness.* The skewness is an index of the difference between the shape of a cell and that of an equilateral cell with an equivalent volume. This parameter ranges between 0 and 1 and the higher is the skewness, the lower is the stability and accuracy of the solution [54].

- *Orthogonal quality.* To compute the orthogonal quality of a cell, vector mechanics is used. This parameter can assume values from 0 to 1. Grids with an orthogonal quality close to 1 guarantee higher stability and accuracy [54].

- *Element quality.* The element quality depends on the ratio of the volume of the cell to the square root of the cube of the sum of the square of the edge lengths.

$$\frac{V}{\sqrt{\left(\sum_{i=1}^{n} l_i^2\right)^3}} \tag{4.1}$$

  It ranges between 0 and 1. A high element quality is desirable [54].

After assessing the quality of the computational grid, a key step of all the CFD studies is the understanding of the number of cells required to discretize the physical domain. With an increase in the number of grid elements, the solution of the discretized equations is expected to approach the exact solution of the corresponding differential equation. On the other hand, a too fine mesh leads to a high computational cost and an unacceptable long time to get results from the simulation.

Therefore, an optimum number of cells must be found in order to get a solution which does not depend on the coarseness of the mesh in a reasonable time.

4.2 Equation discretization

The discretization process is applied to each element within the computational domain, resulting in an algebraic relationship that links the variable's value within a cell to the values of the same variable in neighboring cells. This algebraic equation is obtained by discretizing the differential equation. For a given differential equation, there is no unique discretized formulation, although it is expected that all types of discretization techniques, with a sufficiently large number of grid elements, converge to the same solution. The variations in discretization types stem from differences in profile assumptions and derivation methods. The main discretization methods include the Finite Volume Method, the Finite Element Method, and the Finite Difference Method.

4.2.1 The Finite Volume Method

The Finite Volume Method (FVM) has played a notably significant role in simulating fluid flow problems using CFD tools. In the finite volume method, the discretization of the equation involves an initial step of integrating the differential equation over a control volume or cell, resulting in a semi-discretized form of the equation. Subsequently, the ultimate discretized form is obtained by approximating the variation of the dependent variable between grid elements.

The interest in this method stems from its inherently conservative nature. Indeed, the conservation of the extensive properties, like momentum, mass and energy, is guaranteed even using a coarse mesh grid, with few cells, inadequate to efficiently describe what happens within the system.

To understand how the FVM is implemented, the transport equation of the generic extensive property Φ can be considered:

$$\frac{\partial}{\partial t}(\rho\Phi) + \nabla \cdot (\rho \mathbf{u}\Phi) = \nabla \cdot (\Gamma^{\Phi}\nabla\Phi) + Q^{\Phi} \tag{4.2}$$

where Γ^{Φ} represents the generic diffusivity coefficient $[m^2/s]$ and Q^{Φ} is the source term of the transport equation.

It is possible to apply the semi-discretization of the equation by integrating the conservation law over the finite volumes:

$$\int_V \frac{\partial}{\partial t}(\rho\Phi)\, dV + \int_V \nabla \cdot (\rho \mathbf{u}\Phi)\, dV = \int_V \nabla \cdot (\Gamma^{\Phi}\nabla\Phi)\, dV + \int_V Q^{\Phi}\, dV \tag{4.3}$$

The convective and the diffusive term can be transformed into surface integrals by the Gauss divergence theorem:

$$\int_V \frac{\partial}{\partial t}(\rho\Phi)\,dV + \int_S (\rho\mathbf{u}\Phi)\mathbf{n}\,dS = \int_S (\Gamma^\Phi \nabla\Phi)\mathbf{n}\,dS + \int_V Q^\Phi\,dV \tag{4.4}$$

where $\mathbf{n}$ is the vector perpendicular to the surface of the control volume.

It's important to note that following this process, the equation still gives an exact solution. However, in order to solve the flow numerically, it is necessary to further discretize the volumes and surface integrals. The examinations of all the terms of the transport equation are conducted independently of each other, given that they embody distinct physical phenomena. Consequently, from a numerical standpoint, they must be treated differently, necessitating unique interpolation profiles and considerations for each.

Diffusion term

In order to lighten up the discussion, a simple case with a regular Cartesian grid will be considered, and the compass notation will be used to name the cells.

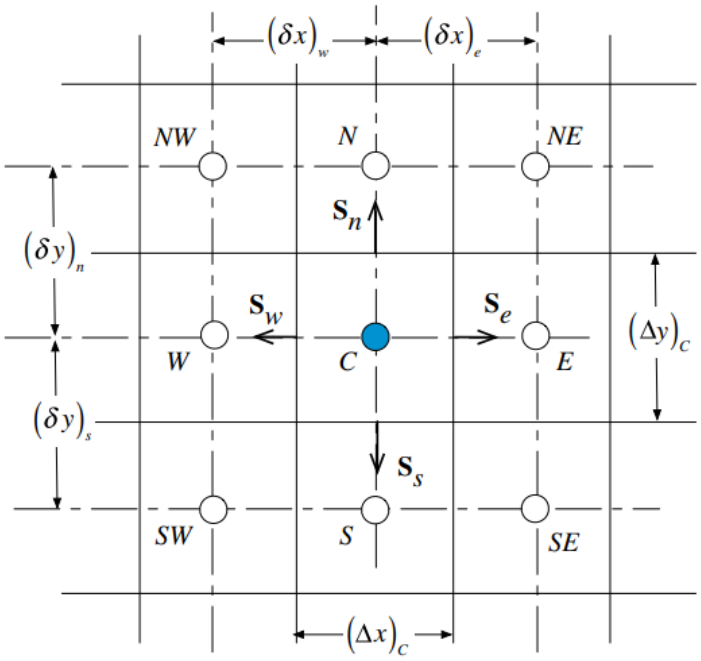

Figure 4.3: A regular Cartesian grid. [51]

Firstly, the diffusion term can be expressed as a generic diffusion flux:

$$-\Gamma^{\Phi}\nabla\Phi = \mathbf{J}^{\Phi,D} \tag{4.5}$$

Focusing on cell C in Fig. 4.3, the generic flux $\mathbf{J}^{\Phi,D}$ can be broken down into individual flux terms between cell C and the adjacent cells.

$$\mathbf{J}^{\Phi,D} = (-\Gamma^{\Phi}\nabla\Phi)_e \cdot \mathbf{S}_e + (-\Gamma^{\Phi}\nabla\Phi)_w \cdot \mathbf{S}_w + (-\Gamma^{\Phi}\nabla\Phi)_n \cdot \mathbf{S}_n + (-\Gamma^{\Phi}\nabla\Phi)_s \cdot \mathbf{S}_s \tag{4.6}$$

Introducing the vectors normal to the faces of the cells, the surface vectors can be expressed in the following way:

$$\begin{aligned} \mathbf{S}_e = +(\Delta y)_e\,\mathbf{i} = ||\mathbf{S}_e||\,\mathbf{i} = S_e\mathbf{i};\;\; \mathbf{S}_w = -(\Delta y)_w\,\mathbf{i} = -||\mathbf{S}_w||\,\mathbf{i} = -S_w\mathbf{i}; \\ \mathbf{S}_n = +(\Delta x)_n\,\mathbf{j} = ||\mathbf{S}_n||\,\mathbf{j} = S_n\mathbf{j};\;\; \mathbf{S}_s = -(\Delta x)_s\,\mathbf{j} = -||\mathbf{S}_s||\,\mathbf{j} = -S_s\mathbf{j} \end{aligned} \tag{4.7}$$

Considering the diffusion flux through the east face of the cell as an example, it is possible to reformulate $\mathbf{J}_e^{\Phi,D}$ as follows:

$$\mathbf{J}_e^{\Phi,D} = (-\Gamma^{\Phi}\nabla\Phi)_e \cdot \mathbf{S}_e = -\Gamma^{\Phi}S_e\left(\frac{\partial\Phi}{\partial x}\mathbf{i} + \frac{\partial\Phi}{\partial y}\mathbf{j}\right)_e \cdot\ \mathbf{i} = -\Gamma^{\Phi}(\Delta y)_e\left(\frac{\partial\Phi}{\partial x}\right)_e \tag{4.8}$$

An input profile is required to depict how Φ changes between the centroids of the two elements that share the east face. Assuming a linear variation of Φ between cell centroids, the gradient along the $\mathbf{i}$ direction at face e can be written in the following manner:

$$\left(\frac{\partial\Phi}{\partial x}\right)_e = \frac{\Phi_E - \Phi_C}{(\delta x)_e} \tag{4.9}$$

where $(\delta x)_e$ is the distance between the two cell centroids $[m]$.

Substituting this term in Equation (4.8), the diffusion term assumes the following discretized form:

$$\mathbf{J}_e^{\Phi,D} = -\Gamma^{\Phi}(\Delta y)_e\frac{\Phi_E - \Phi_C}{(\delta x)_e} \tag{4.10}$$

Convection term

While the convection term may appear straightforward, its discretization has posed numerous challenges that researchers have grappled with for decades. Their efforts have brought insights into the obstacles impeding its discretization, leading to the creation of a large number of convection schemes.

In this paragraph, a one-dimensional grid, like the one shown in Fig. 4.4, will be considered, to make the discretization procedure easier to understand. In particular, the focus will be on the description of the upwind schemes, used in the current hydrodinamic study.

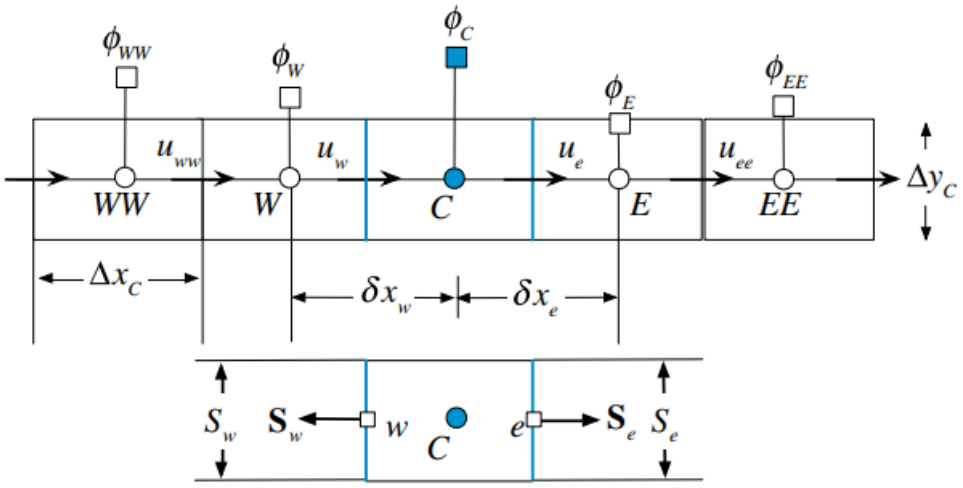

Figure 4.4: One-dimensional grid. [51]

Starting from the semi-discretized equation of a simple convection-diffusion problem, expressed as

$$\int_{V_C} [\nabla \cdot (\rho \mathbf{u} \Phi) - \nabla \cdot (\Gamma^{\Phi} \nabla \Phi)] \, dV = 0 \tag{4.11}$$

it is possible to reformulate the transport equation in terms of convection and diffusion fluxes:

$$\int_{V_C} \nabla \cdot (\mathbf{J}^{\Phi,C} + \mathbf{J}^{\Phi,D}) \, dV = 0 \tag{4.12}$$

where $\mathbf{J}^{\Phi,C} = \rho \mathbf{u} \Phi$ and $\mathbf{J}^{\Phi,D} = -\Gamma^{\Phi} \nabla \Phi$

Applying Gauss Divergence theorem and considering a fluid moving along vector **i**, parallel to the one dimensional grid, the volume integral is transformed as shown:

$$\int_{V_C} \nabla \cdot (\mathbf{J}^{\Phi,C} + \mathbf{J}^{\Phi,D})\, dV = \int_{\partial V_C} \left[\rho u \Phi \mathbf{i} - \Gamma^{\Phi} \frac{d\Phi}{dx} \mathbf{i} \right] dS \tag{4.13}$$

The expanded version of the surface integral can be obtained noting that **i** is the normal vector of the east face of cell C.

$$\left[(\rho u \Delta y \Phi)_e - \left(\Gamma^{\Phi} \frac{d\Phi}{dx} \Delta y \right)_e \right] - \left[(\rho u \Delta y \Phi)_w - \left(\Gamma^{\Phi} \frac{d\Phi}{dx} \Delta y \right)_w \right] = 0 \tag{4.14}$$

The fluid velocity u at the cell faces is known and $\frac{d\Phi}{dx}$ can be discretized as in Equation (4.9). The challenge lies in determining the discretization approach for the face values Φ_e and Φ_w in relation to the values at neighboring nodes.

The upwind scheme A linear and symmetric profile, as the one suggested by the central difference scheme, distributes equal weights to the two nodes that share the face, without showing any directional bias. This is fitting for non-directional phenomena like diffusion, but it doesn't correctly describe fluids moving with a bulk motion. In contrast, the upwind scheme essentially replicates the core principles of convection by linking the cell face value to the upwind nodal value, thereby accounting for the flow direction.

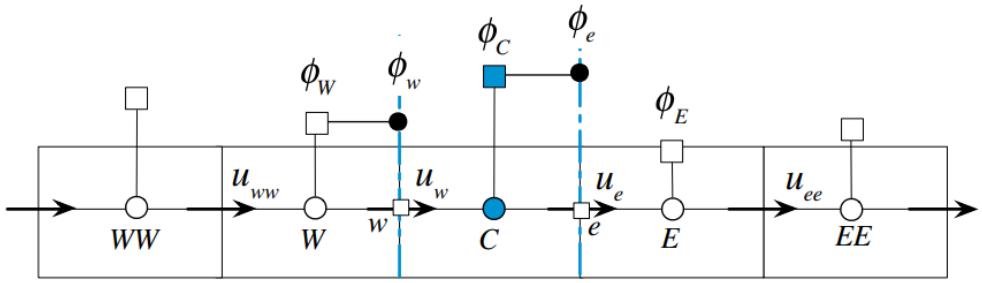

Figure 4.5: The upwind scheme profile. [51]

Referring to Fig. 4.5, Φ_e and Φ_w are modeled as follows:

$$\Phi_e = \begin{cases} \Phi_C, & \dot{m}_e > 0 \\ \Phi_E, & \dot{m}_e < 0 \end{cases} \quad \text{and} \quad \Phi_w = \begin{cases} \Phi_C, & \dot{m}_w > 0 \\ \Phi_W, & \dot{m}_w < 0 \end{cases} \tag{4.15}$$

where $\dot{m}_e$ and $\dot{m}_w$ are the mass flow rates at the east and west face $[kg/s]$, which can be written as

$$\begin{aligned} \dot{m}_e &= (\rho \mathbf{u} \cdot \mathbf{S})_e = (\rho u S)_e = (\rho u \Delta y)_e \\ \dot{m}_w &= (\rho \mathbf{u} \cdot \mathbf{S})_w = (\rho u S)_w = (\rho u \Delta y)_w \end{aligned} \tag{4.16}$$

Therefore, the convection fluxes at the east and west faces of cell C can be formulated as follows:

$$\begin{aligned} \dot{m}_e \Phi_e &= ||\dot{m}_e, 0|| \Phi_C - ||-\dot{m}_e, 0|| \Phi_E \\ \dot{m}_w \Phi_w &= ||\dot{m}_w, 0|| \Phi_C - ||-\dot{m}_w, 0|| \Phi_W \end{aligned} \tag{4.17}$$

where the expression $||a, b||$ takes the maximum value between a and b.

Substituting the discretized form of the convection and diffusion terms in Equation (4.14), the following discretized transport equation can be obtained:

$$a_C \Phi_C + a_E \Phi_E + a_W \Phi_W = 0 \tag{4.18}$$

where

$$\begin{aligned} a_C &= ||\dot{m}_e, 0|| + ||\dot{m}_w, 0|| + \Gamma_e^\Phi \frac{S_e}{\delta x_e} + \Gamma_w^\Phi \frac{S_w}{\delta x_w} \\ a_E &= -||-\dot{m}_e, 0|| - \Gamma_e^\Phi \frac{S_e}{\delta x_e} \\ a_W &= -||-\dot{m}_w, 0|| - \Gamma_w^\Phi \frac{S_w}{\delta x_w} \end{aligned} \tag{4.19}$$

It is evident that the upwind scheme results in negative coefficients for neighboring cells. Moreover, a_C is given by

$$a_C = -(a_E + a_W) \tag{4.20}$$

ensuring the boundedness property to the numerical method. However, it is easily demonstrated that the accuracy of the method can be improved with higher-order schemes.

For a simple case with a uniform one-dimensional grid, cell face values can be written as functions of the cell centroids values, through one dimensional Taylor series expansions.

$$\Phi_e = \Phi_C + (\frac{\partial \Phi}{\partial x})(x_e - x_C) + ...$$
$$\Phi_w = \Phi_W + (\frac{\partial \Phi}{\partial x})(x_w - x_W) + ... \tag{4.21}$$

Imposing values at the cell faces equal to the values at the cell centroids, as shown in Equation (4.15), the first terms of the Taylor series expansions to be neglected are $(\frac{\partial \Phi}{\partial x})(x_e - x_C)$ and $(\frac{\partial \Phi}{\partial x})(x_w - x_W)$. Hence, a truncation error proportional to $\Delta x/2$, where Δx is the element size, causes the upwind scheme to be a first-order method.

Substituting Equation (4.21) in Equation (4.14), it is possible to notice how the neglected term $(\frac{\partial \Phi}{\partial x})(\frac{\Delta x}{2})$ is further multiplied by $\rho\mathbf{u}$. Therefore, it is clear that the truncation error takes the form of a diffusivity which, being dependent on the size of the cell, is called numerical diffusion $[kg/(m * s)]$.

$$\Gamma^{\Phi}_{truncation} = \rho u \frac{\Delta x}{2} \tag{4.22}$$

This streamwise diffusion diminishes the accuracy of the solution by influencing the magnitude of the diffusion coefficient. The convection and diffusion equation reflects an effectively modified value of the diffusion effects, and it is evident that in order to mitigate streamwise numerical diffusion, a higher-order approximation of the convection term and a sufficiently small grid size are necessary. However, for the sake of completeness, it is also important to underline the contribution of this term to stabilize the solution of the transport equation.

Higher order schemes Many efforts have been focused on finding new models capable of describing the convective term, ensuring greater accuracy and unconditional stability. One result of these studies is the Second Order Upwind scheme, which uses a linear profile to extrapolate the generic value at the considered cell face f from the centroids value of cell C and the upwind cell U.

$$\Phi_f = \frac{3}{2}\Phi_C - \frac{1}{2}\Phi_U \tag{4.23}$$

This linear profile produces a second order accurate solution with a numerical diffusion proportional to Δx^2.

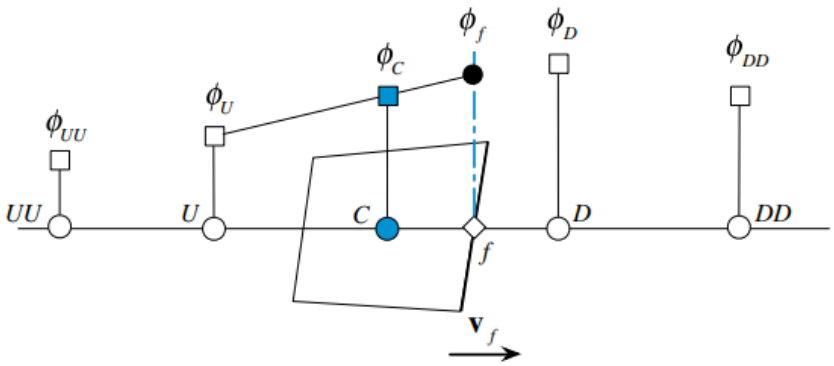

Figure 4.6: The Second Order Upwind scheme profile. [51]

Another widely used numerical method is the QUICK (Quadratic Upstream Interpolation for Convective Kinematics) scheme, which calculates the cell face value interpolating three centroids values by using a quadratic polynomial.

$$\Phi_f = \frac{6}{8}\Phi_C + \frac{3}{8}\Phi_D - \frac{1}{8}\Phi_U \tag{4.24}$$

This interpolation scheme produces a third order accurate approximation and a truncation error proportional to Δx^3.

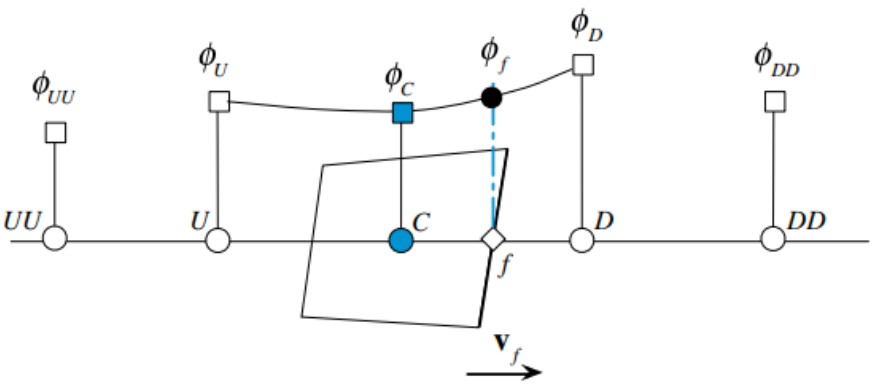

Figure 4.7: The QUICK scheme profile. [51]

Source term - Pressure discretization

The CFD study of interest requires the setting of a pressure interpolation scheme, able to compute the pressure values at the faces of the cells. Pressure field represents a source term in the momentum transport equation and its discretization may be done choosing between a large number of schemes.

The PRESTO! (PREssure STaggering Option) scheme is used in the current study. This interpolation option employs the discrete continuity equation to compute the pressure field on a mesh that undergoes a geometric shift, aligning the new cell centers with the locations where the faces of the original mesh are positioned (staggered grid). Consequently, the pressures on the faces become known in this reconfigured mesh [30, 52].

Transient term

Temporal discretization involves establishing a time coordinate, in addition to the spatial coordinate, to evaluate the integral of the transient term. Beginning with an initial condition at time $t = t_0$, the solution algorithm advances forward to compute a solution at the subsequent time step. The solution obtained becomes the initial condition for the next time step and the iterative process continues until the desired time is reached.

To highlight the presence of the transient term, it is possible to express the transport equation of the generic variable Φ as follows:

$$\frac{\partial(\rho\Phi)}{\partial t} + L(\Phi) = 0 \tag{4.25}$$

where $L(\Phi)$ is a spatial operator that incorporates all non-transient terms.

Integrating the transport equation over the single cell C of the domain gives

$$\int_{V_C} \frac{\partial(\rho\Phi)}{\partial t}\, dV + \int_{V_C} L(\Phi)\, dV = 0 \tag{4.26}$$

and after a spatial discretization, the expression can be written as

$$\frac{\partial(\rho_C\Phi_C)}{\partial t} V_C + L(\Phi_C^t) = 0 \tag{4.27}$$

where $L(\Phi_C^t)$ is the discretized spatial operator at some reference time t and V_C is the volume of the cell of interest.

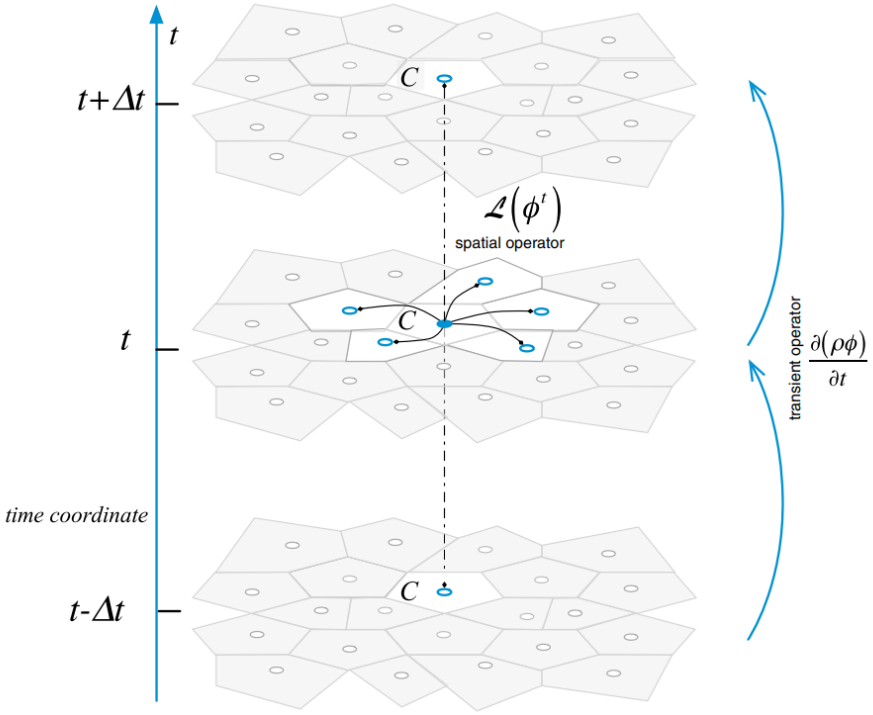

Figure 4.8: Transient and spatial operators. [51]

To discretize the transient term, the integration of $\frac{\partial(\rho\Phi)}{\partial t}$ is carried out over a temporal element and then transformed into face fluxes. Adopting a finite volume approach, a methodology similar to that applied in convection schemes is used, with the only difference that the discretization is conducted along the transient axes.

Integration of Equation (4.27) over the time interval $[t - \Delta t/2, t + \Delta t/2]$ gives

$$\int_{t-\Delta t/2}^{t+\Delta t/2} \frac{\partial(\rho_C \Phi_C)}{\partial t} V_C \, dt + \int_{t-\Delta t/2}^{t+\Delta t/2} L(\Phi_C) \, dt = 0 \tag{4.28}$$

The semi-discretized form of Equation (4.28) is given by considering V_C as a constant, expressing the first integral in terms of face fluxes and assessing the second term as a volume integral with the mid point rule.

$$\frac{(\rho_C \Phi_C)^{t+\Delta t/2} - (\rho_C \Phi_C)^{t-\Delta t/2}}{\Delta t} V_C + L(\Phi_C^t) = 0 \tag{4.29}$$

As already seen for the spatial discretization, it is essential to establish an interpolation profile that relates the face values $(t - \Delta t/2, t + \Delta t/2)$ to the element values $(t, t - \Delta t)$. Regardless of the chosen profile, the flux will be linearized based on old and new values. However, it is evident that the selection will impact the accuracy and robustness of the method.

First order implicit Euler scheme The transient scheme used by the current CFD study is a first order interpolation profile which sets the value of the property $\rho\Phi$ at the face equal to the value assumed by the variable at the centroid of the upwind element.

Therefore, Equation (4.29) is discretized as follows:

$$\frac{(\rho_C \Phi_C)^t - (\rho_C \Phi_C)^{t-\Delta t}}{\Delta t} V_C + L(\Phi_C^t) = 0 \tag{4.30}$$

where

$$\begin{aligned} (\rho_C \Phi_C)^{t+\Delta t/2} &= (\rho_C \Phi_C)^t \\ (\rho_C \Phi_C)^{t-\Delta t/2} &= (\rho_C \Phi_C)^{t-\Delta t} \end{aligned} \tag{4.31}$$

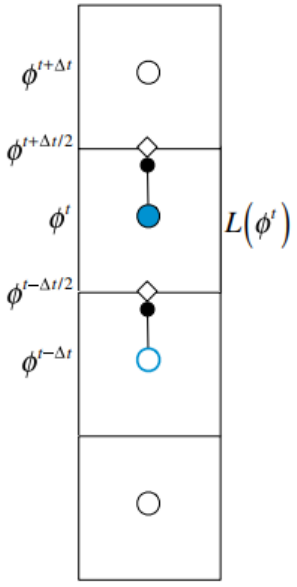

Figure 4.9: First order implicit Euler scheme. [51]

As already discussed for the convective term, a first order scheme may lead to a lack of accuracy, because of a numerical diffusion term which is expressed as follows:

$$\left(\frac{\Delta t}{2}\right) \frac{\partial^2(\rho\Phi)}{\partial t^2}\bigg|_t \tag{4.32}$$

This numerical diffusion term is proportional to $\Delta t/2$ and, although the method is unconditionally stable, a sufficiently small time step is required to not produce an erroneously stationary result.

The choice of the time step size is linked to the Courant number (CFL). The determination of the time step relies on the fluxes within each cell, following the general principle that the time step should be shorter than the time required for transport past the cell. Therefore, for a convection-diffusion problems,

$$\Delta t < CFL\, min\left(\frac{\rho\Delta x^2}{\Gamma}, \frac{\Delta x}{u}\right) \tag{4.33}$$

The first order implicit method should be stable for all time steps. However, due to nonlinearities present in the transport equations, a maximum initial CFL condition equal to 5 is suggested [52].

To sum up, it is possible to gather in a single table all the discretization schemes used by the solver to perform the hydrodynamic study.

Table 4.1: Solution methods.

Spatial discretization	
Gradient	Least Squares Cell Based
Pressure	PRESTO!
Momentum	Second Order Upwind
Volume fraction	QUICK
Turbulent kinetic energy	First Order Upwind
Turbulent dissipation rate	First Order Upwind
Temporal formulation	
First Order Implicit	

4.3 Solution of the algebraic equations

The outcome of the discretization process yields a system of linear equations represented as

$$A\Phi = b \tag{4.34}$$

where Φ contains the unknown values located at the centroids of the grid cells. The coefficients of the unknown variables in matrix A are derived from the discretization procedure and the mesh geometry. Meanwhile, vector b encompasses all sources, constants, boundary conditions, and non-linearizable components. The expanded form of Equation (4.34) is given by

$$\begin{bmatrix} a_{11} & a_{12} & \dots & a_{1N-1} & a_{1N} \\ a_{21} & a_{22} & \dots & a_{2N-1} & a_{2N} \\ \vdots & \vdots & \ddots & \vdots & \\ a_{N1} & a_{N2} & \dots & a_{NN-1} & a_{NN} \end{bmatrix} \begin{bmatrix} \Phi_1 \\ \Phi_2 \\ \vdots \\ \Phi_N \end{bmatrix} = \begin{bmatrix} b_1 \\ b_2 \\ \vdots \\ b_N \end{bmatrix} \tag{4.35}$$

Each row in the matrix corresponds to a discretized transport equation defined over a specific cell of the computation grid, and the non-zero coefficients are related to the neighbors of that particular element. Given that a cell is connected to only a limited number of neighbors, a substantial portion of the coefficients takes on zero values. Consequently, the resulting A matrix is consistently sparse. Moreover, if the geometry is discretized with a structured grid system, all non-zero elements will be aligned along a few diagonals of the matrix A. Therefore, techniques for efficiently solving such systems should leverage this inherent sparsity.

Direct methods are not suitable to solve systems of equations when the coefficient matrix is sparse. In addition, given the highly nonlinear nature of flow problems, the coefficients resulting from their linearization process tend to be solution-dependent. Due to these factors, iterative methods are better aligned with the requirements of such applications, demanding lower computational cost per iteration and reduced memory usage. Utilizing iterative algebraic solvers, the solution algorithm is repeatedly applied until a predefined level of convergence is reached.

4.3.1 The Gauss-Seidel algorithm

Several commercial CFD codes, including Ansys Fluent, use some variant of the Gauss–Seidel algorithm to solve linear systems of equations. The iterative formula for this numerical method is given by

$$\Phi_i^{(n)} = \frac{1}{a_{ii}} \left(b_i - \sum_{j=1}^{i-1} a_{ij} \Phi_j^{(n)} - \sum_{j=i+1}^{N} a_{ij} \Phi_j^{(n-1)} \right), \quad i = 1, 2, 3, ..., N \tag{4.36}$$

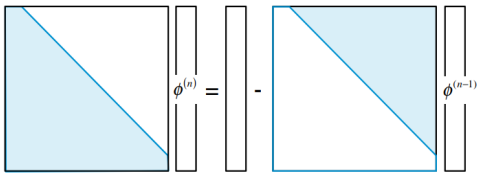

Figure 4.10: Representation of the Gauss-Seidel method. [51]

In order to use this iterative method, it becomes necessary to establish an initial guess of the property of interest Φ in all the cells of the domain. After the initialization step, the process commences with solving Φ_1. Subsequently, when determining Φ_2, the calculated value of Φ_1 and the initial guess for Φ_3 are employed. Therefore, the solver always uses the latest available estimate of Φ in the cells of interest, overwriting the previous values. This iterative approach continues, until numerical values of Φ in all cells are found. However, a notable challenge arises due to the interdependence of, for example, Φ_2 on Φ_1 and Φ_3; consequently, when a new value of Φ_3 is computed, the equation for Φ_2 is no longer satisfied. As a result, the entire procedure necessitates repeated iterations until convergence is reached [52].

In Ansys Fluent, the convergence criteria is set by the user as a scaled residual. Considering the discretized transport equation of Φ at a cell C,

$$a_C \Phi_C = \sum_{nb} a_{nb} \Phi_{nb} + b \tag{4.37}$$

where nb stands for "neighbors", the scaled residual R^{Φ} can be expressed as follows:

$$R^{\Phi} = \frac{\sum_{cellsC} | \sum_{nb} a_{nb} \Phi_{nb} + b - a_C \Phi_C |}{\sum_{cellsC} |a_C \Phi_C|} \tag{4.38}$$

This term represents the imbalance in Equation (4.37) over all the cells present in the computational grid. The denominator term represents a scaling factor useful to assess the imbalance considering the flow rate of Φ through the domain [30].

In this hydrodynamic study, the convergence criteria of all the computed properties is fixed at 0.001.

Under-relaxation factors

Due to the nonlinearities present in transport equations, under-relaxation factors are typically used to avoid divergence of the solving procedure. The under-relaxation factor α can be defined as

$$\Phi_{new} = \alpha\Phi_{solver} + (1 - \alpha)\Phi_{old} \tag{4.39}$$

where Φ_{solver} is the value computed at the cell, Φ_{old} is the previous value assigned to the cell centroid, used to calculate Φ_{solver}, and Φ_{new} is the actual value assigned to the element.

These coefficients range between 0 and 1. Therefore, a value of α close to 1 implies that the newly calculated value will be strongly influenced by the solved value. Each conservation equation is associated with its own under-relaxation factor, which can be modified during the solving process. A careful choice of these factors holds significant practical importance. Indeed, selecting an under-relaxation factor that is too low may lead to unnecessarily long computational times, while an excessively large value may result in a divergent solution [52].

The coefficients employed by Ansys Fluent in the current study are listed below.

Table 4.2: Under-relaxation factors.

Property	**Under-relaxation factor**
Pressure	0.15
Density	0.75
Body forces	0.75
Momentum	0.3
Volume fraction	0.3
Granular temperature	0.15
Turbulent kinetic energy	0.3
Turbulent dissipation rate	0.3
Turbulent viscosity	0.6

4.3.2 The Multigrid method

Given that the Gauss–Seidel algorithm determines the cell values solely based on the values of neighboring cells, this solver shows a high efficiency in miti-

gating local errors in the solutions. However, certain scenarios may necessitate the rapid transmission of information across the domain, like a sudden increase in pressure in a specific region, which instantaneously impact the entire domain [52].

To handle this potential problem, Ansys Fluent solves the sets of algebraic equations using a Gauss-Seidel algorithm in conjunction with an algebraic multigrid scheme (AMG).

The algebraic multigrid method (AMG)

The multigrid strategy uses a series of coarser grid levels to get a faster transfer of the corrections across the domain, allowing a reduction of the number of iterations to get a converged solution. The AMG method is particularly well-suited for application on unstructured meshes because it formulates the coarse-level equations without relying on any geometry or re-discretization on the coarse levels. The key benefit is that there is no need to create or store coarse meshes, and there is no requirement to assess fluxes or source terms on the coarse levels [30].

Information is transported from coarse to finer grid levels through a recursive procedure that moves through the grid hierarchy. Four types of cycles can be used in Ansys Fluent. The V-cycle, which requires a lower number of steps to be completed and is available for the AMG scheme, is examined, to understand the logic behind the multigrid method [30]. The following steps can be easily followed looking at Figure 4.11.

1. Iterations are performed at the finest grid level. A Gauss-Seidel algorithm is used to reduce the high wave-number components of errors. The remaining errors can be transmitted to the coarser grid level.

2. Restriction is done from a finer mesh level to a coarse mesh level.

3. The error is reduced by performing a specified parameter (β_2), which is different for every multigrid scheme.

4. The correction obtained at the coarse grid level is interpolated and added to the solution at the finer mesh level.

5. Iterations are performed to remove the high wave-number errors generated at the coarser grid levels. These iterations refers to a number of post-relaxation sweeps (β_3), which can be different from method to method.

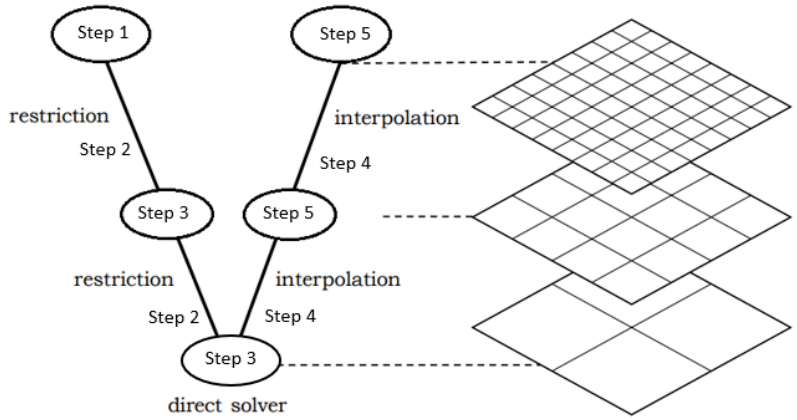

Figure 4.11: Schematic representation of the V-cycle in a multigrid method.

4.3.3 Solver algorithm for Navier-Stokes equations

The main model equations to solve, as mentioned in Section 3.2.1, are the Navier-Stokes equations and the continuity equations. Considering a simpler case with a single fluid and a pressure gradient as the only generation term, these conservation laws can be reformulated as follows:

$$\frac{\partial \rho u_i}{\partial t} + \frac{\partial \rho u_i u_j}{\partial x_j} = \frac{\partial}{\partial x_j}\left(\mu \frac{\partial u_i}{\partial x_j}\right) - \frac{\partial P}{\partial x_i} \tag{4.40}$$

$$\frac{\partial \rho}{\partial t} + \frac{\partial \rho u_j}{\partial x_j} = 0 \tag{4.41}$$

The unknowns of these equations are given by the three components of velocity (u_x, u_y, u_z) and the pressure P, which could be potentially solved through the four equations available. However, there are no equation to solve the pressure field. Meanwhile the velocity components can be solved through the Navier-Stokes equations, the continuity equation represents only a restriction on the x, y and z components of the velocity. Another difficulty of the resolution of these equation arise from the non-linearity of the convection term. Moreover, an equation of state may not be available to compute pressure in case of incompressible and isothermal flows.

The SIMPLE algorithm

To deal with these difficulties, a pressure-based solver can be used. In particular, the current CFD study employs the SIMPLE (Semi-Implicit Method for Pressure-Linked Equations) algorithm for pressure-velocity coupling. The following discussion refers to the notions presented by Andersson et. al in *Computational Fluid Dynamics for Engineers*.

The key strategies of the SIMPLE algorithm are

- the derivation of an equation for pressure from the momentum and the continuity equations,
- the derivation of a corrector for the velocity field, in order to satisfy the continuity equation.

An equation for pressure can be derived by applying the divergence operation to the Navier-Stokes equation. In this way, Equation (4.40) yields

$$\frac{\partial^2}{\partial x_i \partial t}(\rho u_i) + \frac{\partial^2}{\partial x_i \partial x_j}(\rho u_i u_j) = \frac{\partial^2}{\partial x_i \partial x_j}\left(\mu \frac{\partial u_i}{\partial x_j}\right) - \frac{\partial^2 P}{\partial x_i \partial x_i} \tag{4.42}$$

Assuming constant density and constant viscosity, the transient term and the diffusion term can be expressed as follows:

$$\begin{aligned} \frac{\partial}{\partial x_i}\left(\frac{\partial \rho u_i}{\partial t}\right) &= \frac{\partial}{\partial t}\left(\frac{\partial \rho u_i}{\partial x_i}\right) \\ \frac{\partial}{\partial x_i}\left[\frac{\partial}{\partial x_j}\left(\mu \frac{\partial u_i}{\partial x_j}\right)\right] &= \frac{\partial}{\partial x_j}\left[\frac{\partial}{\partial x_j}\left(\mu \frac{\partial u_i}{\partial x_i}\right)\right] \end{aligned} \tag{4.43}$$

Moreover, knowing the continuity equation can be expressed as

$$\frac{\partial u_i}{\partial x_i} = 0 \tag{4.44}$$

in the condition of constant density, Equation (4.42) gives Poisson equation for incompressible fluids, which can be used as a direct equation to find the pressure field.

The solution process of the SIMPLE algorithm requires an initialization of the velocity field and pressure. The starting guess of pressure is used to calculate the velocity components from Navier-Stokes equations. Since the initial value of pressure may not be correct, the velocity components potentially do not satisfy the continuity equation. Consequently, the pressure

field calculated through the Poisson equation is used to correct the velocity field to satisfy this restriction, and the velocity components are solved again from the momentum equations.

Additional transport equations, like turbulence transport equations, can be easily incorporated into the SIMPLE loop, solving them after the velocity corrector.

4.4 Boundary conditions

In order to provide reliable and physically acceptable results from a CFD simulation, a correct setting of boundary conditions plays an essential role. Different solutions arise when employing different boundary conditions, despite the consistency of the general equation, and slight modifications in these conditions, due to numerical approximations, can lead to an incorrect result.

Boundary conditions are imposed on boundary elements, which possess one or more faces along the boundary. Three different types of boundary conditions can be imposed in convection-diffusion problems.

- *Dirichlet boundary condition.* It specifies the value of the generic property Φ at the boundary.

$$\Phi_b = \Phi_{specified} \tag{4.45}$$

- *Von Neumann boundary condition.* It specifies the flux of the generic property Φ at the boundary.

$$-(\Gamma^{\Phi}\nabla\Phi)_b \cdot \mathbf{i} = q_b \tag{4.46}$$

- *Mixed boundary condition.* The boundary condition is specified through the setting of a convection transfer coefficient (h_∞) and a value of Φ for the surroundings (Φ_∞). For a boundary cell C, with S_b as boundary face,

$$-(\Gamma^{\Phi}\nabla\Phi)_b \cdot \mathbf{i}S_b = -h_\infty(\Phi_\infty - \Phi)(\Delta y)_C \tag{4.47}$$

For a fluid-dynamic simulation, boundary conditions are set at the inlet and at the outlet of the flow, but also in proximity of the walls of the physical geometry. All these cases are examined in depth in the following paragraphs. The treatment of wall boundaries refers to the work of Andersson et al. *Computational Fluid Dynamics for Engineers* [52].

4.4.1 Wall

Gas phase

The importance of a correct wall treatment lies in the substantial effect wall boundaries have on flow behaviours. A quick change of magnitude of inertial and viscous forces is present from the bulk region to a near-wall region, where viscous effects play a predominant role on transport phenomena. A realizable $k - \epsilon$ turbulence model does not provide a proper description of the flow behaviour close to the walls of the gasifier. Therefore, in order to avoid really dense meshes, able to capture the rapid variation of the flow variables, wall functions are typically adopted to model boundary conditions for mean-velocity components and turbulent quantities.

No-slip condition is widely accepted in CFD simulations. According to this approximation, the relative velocity between the gaseous stream and the physical boundaries is equal to 0 at the gasifier walls. This condition is due to the transfer of momentum from the molecules to the solid walls, when these gaseous particles hit a solid surface. These molecules are subsequently bounced back into the flow, altering the mean velocity of other gaseous molecules close to the wall region, giving rise to a boundary layer.

The thickness δ of this boundary layer strongly depends on the Reynolds number, but three different sub-layers are usually recognised when the near wall region is shaped.

- A *viscous sub-layer* is defined close to the solid wall, where the molecular viscosity plays a dominant role in momentum transfer and the flow can be considered as laminar.
- A *buffer sub-layer* is shaped at a further distance from the solid surface, where the molecular viscosity and the turbulent viscosity are equally important to describe the fluid behaviour.
- A *fully-turbulent sub-layer* is finally defined at even larger distances, where the viscous stresses become negligible compared to the turbulent stresses.

The thickness of these sub-layers can be expressed in terms of wall variables. A first variable which can be defined is the friction velocity u^* $[m/s]$, written as

$$u^* = \sqrt{\frac{\tau_w}{\rho}} \tag{4.48}$$

where τ_w is the wall shear stress $[kg/(m * s^2)]$ and ρ is the density of the fluid $[kg/m^3]$.

Knowing the kinematic viscosity of the fluid, a characteristic wall length l^* $[m]$ can be also calculated.

$$l^* = \frac{\nu}{u^*} \tag{4.49}$$

Through the characteristic velocity and length, scaled variables can be obtained:

$$u+ = \frac{u}{u^*} \tag{4.50}$$

and

$$y+ = \frac{y}{l^*} \tag{4.51}$$

where y is the distance of a physical point from the closest solid surface $[m]$ and u is the velocity magnitude of the fluid in that point $[m/s]$. Expressing the extent of the sub-layers in terms of the scaled length $y+$, it is possible to conclude that

- *Viscous sub-layer*: $0 < y+ < 5$.
- *Buffer sub-layer* $5 < y+ < 30$.
- *Fully-turbulent sub-layer* $30 < y+ < 400$.

These sub-layers can be modeled in different ways depending on the wall functions chosen by the user. The fundamental concept behind this approach is that boundary conditions are not applied at the points of the wall, but they are used at the corresponding first grid points, placed at a higher distance from the surface, as shown in Figure 4.12. In this way, wall functions facilitate the inclusion of rapid variations in flow variables within the near-wall region, without necessitating the resolution of the viscous near-wall region. Moreover, turbulence models do not need to be applied in regions beyond the first grid points, close to the solid surfaces.

To shape the fluid behaviour in the near-wall region, standard wall functions have been used in the current CFD study.

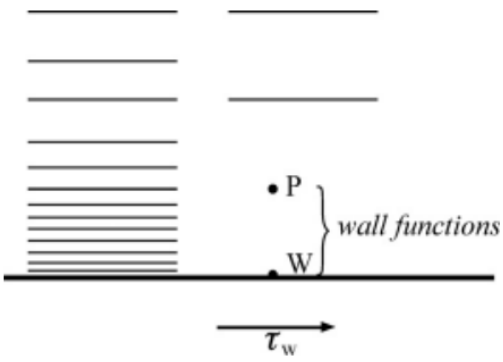

Figure 4.12: Wall-functions approach in a CFD simulation. [52]

Standard wall functions This wall treatment allows the definition of the mean scaled velocity of the fluid as a function of the scaled distance from the solid wall.

$$\langle u \rangle + = f(y+) \tag{4.52}$$

Considering a Cartesian bidimensional coordinate system, the wall shear stress can be written as

$$\tau_w = \tau_{xy} = \rho\nu \frac{d\langle u_x \rangle}{dy} - \rho \langle u_x u_y \rangle \tag{4.53}$$

where u_x and u_y are the velocity components that are parallel and perpendicular to the wall.

In the innermost layer, the wall shear stress highly depends on the viscous effects, which allow Equation (4.53) to be rewritten as follows:

$$\tau_w = \rho\nu \frac{d\langle u_x \rangle}{dy} \tag{4.54}$$

Integrating with respect to y, and assuming the relative velocity between solid surface and the fluid is 0 at the wall, a linear law can be obtained to describe the laminar flow in the viscous sub-layer.

$$\langle u_x \rangle + = y+ \tag{4.55}$$

In particular, the linear law is applied for distances from the wall which respect the condition $y+ < 11.225$.

In the outermost sub-layer, at distances $y+ > 11.225$, the wall shear stress is shaped neglecting the viscous effects, and considering this whole region as a fully-turbulent layer.

$$\tau_w = -\rho\langle u_x u_y \rangle \tag{4.56}$$

By introducing Prandtl's mixing-length model, and integrating with respect to y, a logarithmic velocity profile is obtained to model the considered sub-layer.

$$\langle u_x \rangle + = \frac{1}{\kappa} ln(y+) + B \tag{4.57}$$

where $\kappa \approx 0.42$ is the von Karman constant and $B \approx 5$ is an integration constant.

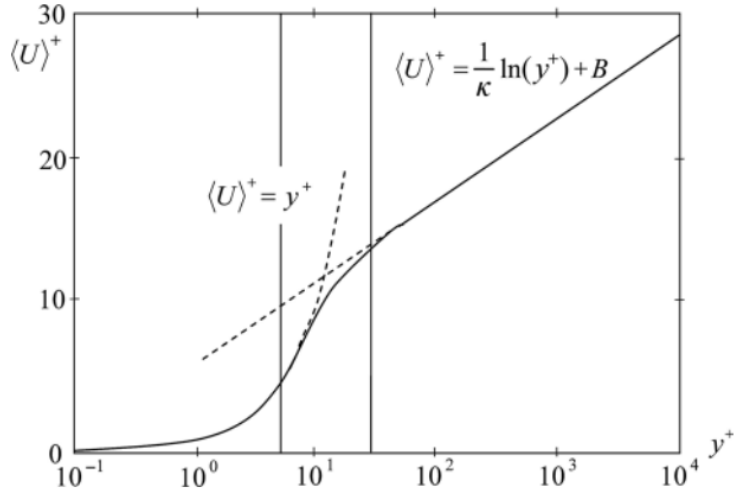

Figure 4.13: Wall treatment according to the Standard wall functions. [52]

In addition to the velocity profiles in the boundary layer, the standard wall functions provide equations for the near-wall turbulent quantities. Equations for k and ϵ are obtained by considering a local equilibrium of the flow, i.e., assuming that the turbulent kinetic energy production equals its dissipation rate.

The use of this type of wall functions requires that each wall-adjacent cell's centroid is located within the log-law region ($30 < y+ < 300$). Moreover, a $y+$ value close to the lower bound of this sub-layer is desirable ($30 < y+ < 100$). This condition will be verified in the following chapter of the thesis project.

Solid phase

An effective description of particle-wall interactions is also critical for an accurate prediction of the hydrodynamics in a fluidized bed reactor [55]. While a no-slip condition is commonly employed to represent the velocity profile of the fluid near the solid surface, a specularity coefficient ϕ is utilized to define the shear condition arising from the interaction between walls and particles. This coefficient can be set from 0 to 1. When $\phi = 0$, a free-slip boundary condition is imposed without the frictional influence of particles on the wall. Conversely, when $\phi = 1$, a no-slip boundary condition is applied, considering the frictional effect of particles on the wall [35].

The specularity coefficient cannot be directly measured, but it must be adjusted on a case-by-case basis until the CFD simulation fits the experimental data. According to Zhong et al. [35], for a bubbling fluidized bed vessel made of glass and aluminium, with glass beads, a specularity coefficient equal to 0.005 gives the best agreement with the experimental results, in terms of solid velocity distribution. This value has been used to carry out additional experimental studies regarding the hydrodynamics of CFB risers [34], and it has been also considered to model the sand particles - walls interactions in CFD simulations [40, 56].

Therefore, a specularity coefficient $\phi = 0.005$ has been used to describe the shear stress between particles and solid walls in the current CFD study. Being all the walls made of the same material, this boundary condition is the same for all the solid surfaces.

4.4.2 Inlet

Gas phase

To establish the boundary conditions for the gas inlet, it is important to delineate some of the approximations, concerning the operating conditions, which have an influence on the physical properties of the fluid:

- *Air as the only gaseous component.* As already mentioned in Section 2.2, the contribution of steam is neglected to carry out the hy-

drodynamic study of the HFB gasifier. No reactions are involved and the air represents the only gaseous component to be modeled.

- *Isothermal conditions.* Since the behaviour of the multiphase flow embodies the focus of the CFD study, the hydrodynamics is examined at room temperature. Due to the absence of chemical reactions and the absence of thermal sinks and thermal sources, the temperature will be constant and equal to 20°C.

- *Absence of a gas distributor.* In order to simplify the geometry, and to lighten the computational cost of the CFD simulation, the presence of a gas distributor at the inlet of the riser has been neglected. Therefore, the airflow enters the gasifier with a uniform velocity and pressure across the whole riser bottom section.

In addition to these approximations, a relatively small pressure drop is considered, in order to model a system in isobaric conditions. This hypothesis permits the setting of a constant air density and a constant air viscosity, as they remain unaffected by changes in temperature or pressure. This assumption requires validation through an examination of the actual pressure drop projected by the fluid dynamic model.

Air density and air viscosity are set depending on the operating pressure of the case of interest and their values are provided by *Perry's Chemical Engineers' Handbook - 9th Edition* [57].

Different air velocities are studied, to observe the effect of this variable on the hydrodynamics of the system. The velocity is always set as normal to the boundary and values from $1\,m/s$ to $2\,m/s$ are considered.

The operating pressure is a second variable whose effect is studied in this work. Target operating pressures are $3\,bar$ and $9.4\,bar$. The operating pressure set at the gas inlet is $0.1\,bar$ higher than the target pressure, in order to avoid backflows.

Considering a case study where the air velocity at the inlet is $1\,m/s$ and the operating pressure is set at $3\,bar$, it's possible to verify the presence of turbulence within the system. Knowing operating temperature and pressure, air density and the air viscosity are easily found, in order to calculate the Reynolds number at the inlet. The diameter D of the bottom section of the riser is also known.

$$Re = \frac{\rho v D}{\mu} \approx 48\,968 >> 2100 \tag{4.58}$$

At higher velocities, the air flow would be even more turbulent and initial guesses of k and ϵ are required by Ansys Fluent to model the turbulence. It becomes crucial to define accurate or realistic boundary conditions, given that the turbulence at the inlet can exert a substantial impact on the flow downstream.

Due to the difficulties linked to the formulation of accurate initial guesses of k and ϵ, Ansys Fluent allows the definition of turbulence through more convenient variables. For all the simulations, the hydraulic diameter D_H $[m]$ and the turbulence intensity I $[-]$ have been chosen to set the turbulence boundary conditions.

- *Hydraulic diameter (D_H).* This property can be easily defined knowing the diameter of the riser section. From the hydraulic diameter, the turbulence length scale l $[m]$ can be easily calculated. This length is directly linked to the size of the energy-containing eddies [54].

- *Turbulence intensity (I).* The turbulence intensity provides a measure of the magnitude of velocity fluctuations in proportion to the average velocity of the fluid.

$$I = \frac{\sqrt{(u')^2}}{\overline{u}} \tag{4.59}$$

  For internal flows, the turbulence intensity of a fully-developed flow can be estimated thanks to the following empirical correlation:

$$I = 0.16(Re_{D_H})^{-1/8} \tag{4.60}$$

  where Re_{D_H} $[-]$ is the Reynolds number obtained by considering the hydraulic diameter, i.e., the diameter of riser section [54].

Solid phase

As mentioned in Section 2.4, since no reactions are involved in the current study, the silica sand grains constitute the entirety of the solid phase in the system, and the presence of biomass pellets will be disregarded.

The solid phase is not introduced with a certain velocity through the inlet section, but it is entirely charged before running hydrodynamic tests.

The silica sand used by Phoenix BioPower has an intrinsic density of 2650 kg/m^3 and 120 kg is the total mass of the bed inventory. The bulk density is equal to 1500 kg/m^3.

From this dataset, the effective volume occupied by the sand particles can be calculated. Additionally, knowing the cross-section of the riser, it is possible to obtain the height of the inert bed before letting the air flowing. The packed bed height at $t = 0\ s$ is approximately 1.591 m. Moreover, a packing bed void fraction equal to 0.434 can be also derived.

The diameter of the sand particles is set as a constant value equal to 250 μm, which represent the mean diameter of the grains composing the bed.

4.4.3 Outlet

Gas phase

Similarly to the gas inlet, boundary conditions are needed at the outlet of the gasifier to model the turbulence.

Knowing the geometry of the cyclone, the hydraulic diameter of the outlet pipe can be easily typed in Ansys Fluent. A preliminary estimate for turbulence intensity is also necessary, and in accordance with Andersson et al. [52], a value of 5% has been selected for all simulations.

The outlet pressure has always been set equal to the target operating pressure and the outlet gas velocity has been defined as normal to the boundary.

Solid phase

For the solid phase, a backflow volume fraction equal to 0 has been set.

Chapter 5

Results and Discussion

5.1 Grid indipendence

The initial phase of the hydrodynamic investigation involves determining the appropriate number of cells to adequately simulate all relevant scenarios. It's imperative for the mesh to be sufficiently dense to avoid yielding a solution dependent on the cell size, thus ensuring an accurate description of the system's physics and providing reliable results for future reactor design considerations. Once the minimum number of cells required to achieve a grid-independent solution has been established, increasing the mesh density further becomes futile. This would only lead to significantly prolonged resolution times without improving the accuracy of the reproduced results.

The mesh indipendence study of the case of interest involves the analysis of four different grids, built on geometries devoid of the orifice, and whose characteristics are summarised in Table 5.1

Table 5.1: Mesh quality of the examined computational grids.

	Grid 1	**Grid 2**	**Grid 3**	**Grid 4**
Number of Cells	1 223 572	1 661 734	2 170 446	2 672 538
Average Element Size $[m]$	0.01	0.009	0.008	0.0075
Average Orthogonal Quality	0.96743	0.96939	0.97061	0.97140
Average Element Quality	0.80297	0,81297	0,80557	0.80685
Average Skewness	0.0828	0.0803	0.0757	0.0745
Average Aspect Ratio	1.8226	1,7724	1.7852	1.7976

The analysis has been conducted by observing the variation of pressure along the axis of the riser, as the cell size decreased. This property was

selected due to the significant interest in the magnitude of pressure drops within this hydrodynamic study. For all four computational grids, the time-averaged pressure has been detected by sampling an interval of 5 seconds, running the simulations with a constant time step of 0.0005 seconds. For this preliminary study, an air flow entering the gasifier at 1 m/s and a desired outlet pressure of 3 bar have been considered. The boundary conditions which have been modified for this particular setting of operating conditions are schematically outlined below:

Table 5.2: Boundary conditions for the grid indipendence study.

Boundary Conditions [1 m/s; 3 bar]	
Air Density $[kg/m^3]$ (Inlet)	3.65
Air Viscosity $[Pa * s]$ (Inlet)	$1.86 * 10^{-5}$
Air Velocity $[m/s]$ (Inlet)	1
Turbulence Intensity [%]	4.148
Inlet Pressure $[Pa]$	310 000
Outlet Pressure $[Pa]$	300 000

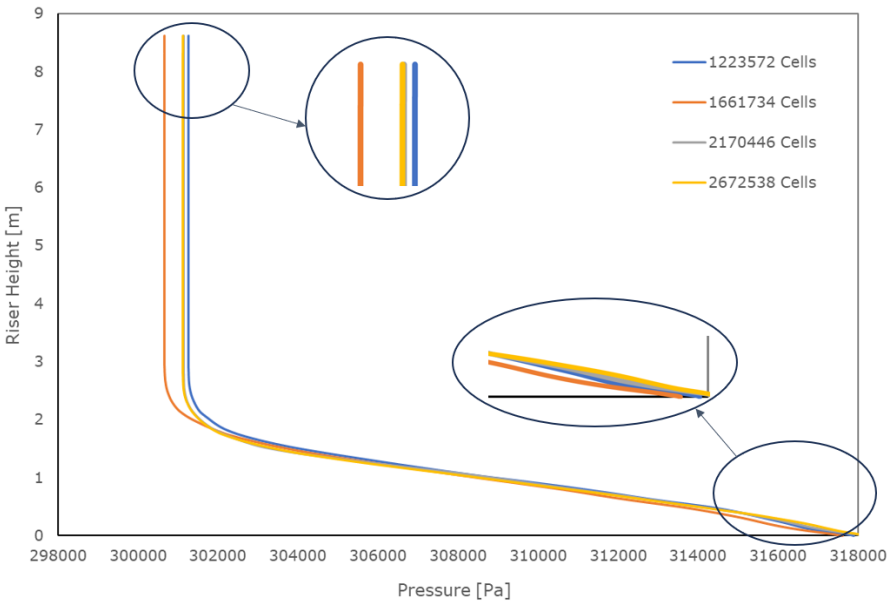

Figure 5.1: Time-averaged pressure along the axis of the riser.

As depicted in Figure 5.1, Grid 3 and Grid 4 yield nearly coincident results. The time-averaged pressure computed by Grid 3 at the riser inlet

stands at 318 182 Pa, only 13 Pa less than the simulation utilizing 2 672 538 cells. Similarly, the pressures recorded at the topmost section of the riser differ by only 16 Pa. However, it is worth noting that even a coarse mesh, with only 1 223 572 cells, produces very similar results to the fine mesh cases. Consequently, an investigation into the time-averaged solid volume fraction along an arbitrary height of the riser has been undertaken. Specifically, the average solid fraction along a horizontal segment, positioned 1.4 meters from the inlet and intersecting the riser axis, was plotted.

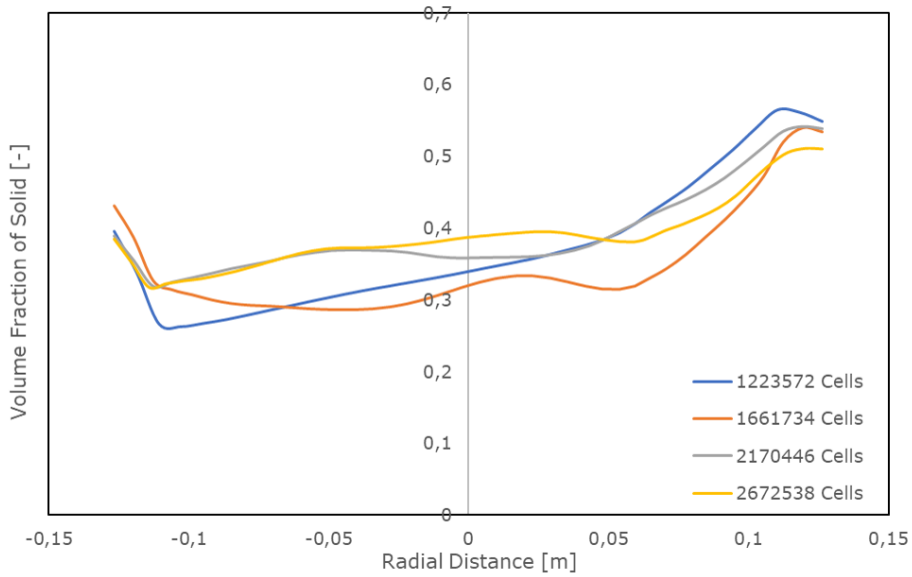

Figure 5.2: Time-averaged volume fraction of solid at 1.4 m above the inlet section.

Figure 5.2 illustrates that, for negative radial distances from the riser axis, in the adopted reference system, Grid 3 and Grid 4 yield results that are nearly identical, while Grid 1 predicts an averaged volume fraction of solid which is approximately 0.06 lower along a significant portion of the segment's length. Larger differences between the predictions of Grids 3 and 4 emerge for positive radial distances, albeit with volume fraction variances not exceeding 0.03 and an analogous trend in the trend lines.

In light of the presented results, it can be inferred that further refinement of the grid does not lead to different results from those obtained. Therefore, it has been decided to use, for future CFD simulations, a computational grid with an average element size equal to 0.008 m, akin to Grid 3.

5.2 Computational cases

The analysis of the influence of the operational conditions of interest on the gasifier's hydrodynamics involves modeling a base case characterized by a specific operating pressure, inlet gas velocity, and a fixed diameter of the solid particles. For convenience, the base case is characterised by the same operating conditions used for the grid independence study. The geometry employed, as well as the models studied thereafter, are not devoid of the orifice, and a grid with an average element size of 0.008 m is generated using the "Fluent Meshing" tool.

Below are the boundary conditions which have been subsequently modified in the other models analysed. For the sake of simplicity, this initial case will be referred to as *Case 0*.

Table 5.3: Boundary conditions for Case 0.

Case 0	
Air Density $[kg/m^3]$ (Inlet)	3.65
Air Viscosity $[Pa * s]$ (Inlet)	$1.86 * 10^{-5}$
Air Velocity $[m/s]$ (Inlet)	1
Turbulence Intensity [%]	4.148
Inlet Pressure $[Pa]$	310 000
Outlet Pressure $[Pa]$	300 000
Particle Diameter $[\mu m]$	250

Starting from *Case 0*, the current study aims to investigate the effect of operating pressure, inlet gas velocity, and solid particle diameter on the gasifier hydrodynamics. Therefore, three additional models have been developed, each varying one operating condition from the initial case, along with all boundary conditions associated with that operating condition.

The first case utilizes a solid bed composed of grains with a constant diameter of 600 μm. This case will be referred to as *Case G*, where letter G stands for *Granular*.

A second case operates at a higher pressure and will be named *Case P*. The desired outlet pressure has been set to 9.4 bar, with the inlet pressure fixed at 9.5 bar. The gas density has been adjusted accordingly, along with the fluid viscosity, although the latter is minimally influenced by a pressure change [57].

Finally, an additional case, named *Case V*, has been modeled with a fluid inlet velocity which is double compared to *Case 0*.

The boundary conditions of interest for the three cases are tabulated below.

Table 5.4: Boundary conditions for the three additional cases.

	Case G	**Case P**	**Case V**
Air Density $[kg/m^3]$ (Inlet)	3.65	11.25	3.65
Air Viscosity $[Pa * s]$ (Inlet)	$1.86 * 10^{-5}$	$1.866 * 10^{-5}$	$1.86 * 10^{-5}$
Air Velocity $[m/s]$ (Inlet)	1	1	2
Turbulence Intensity [%]	4.1480	3.5991	3.8041
Inlet Pressure $[Pa]$	310 000	950 000	310 000
Outlet Pressure $[Pa]$	300 000	940 000	300 000
Particle Diameter $[\mu m]$	600	250	250

The cases, respectively labelled as *Case 0* and *Case G*, have been calculated using a time step of 0.001 s. On the other hand, due to higher expected velocities, the remaining two models have been simulated with a time step of 0.0005 s to ensure computational stability.

For each simulation, the initial 5 seconds of activity have been sampled, and all cases under investigation achieved convergence. At the end of the simulations, a validation of the y+ magnitude at the walls has been performed. In accordance with the constraints imposed by the use of the standard wall functions for wall treatment (see Paragraph 4.4.1), the imposed condition has found to be satisfied.

5.3 Analysis of pressure drops

A preliminary analysis can be carried out by observing the pressure drops recorded in the four individual cases. This data is of practical importance as it shows the initial pressure at which the gasifying agent must be supplied to achieve the target outlet pressure. It is important to emphasize that the higher the predicted pressure drops, the higher the costs required to pressurize the inlet gas.

Figure 5.3 shows the time-averaged pressure drops as a function of the riser height, while the exact inlet pressure values for each case are listed in Table 5.5.

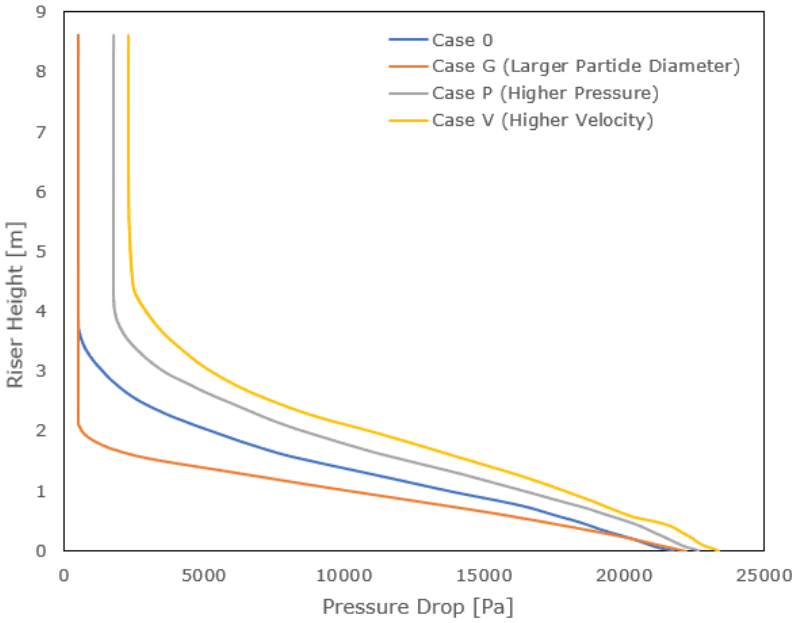

Figure 5.3: Time-averaged pressure drops along the height of the riser.

Table 5.5: Pressures of the inlet gas.

Pressures of the inlet gas	
Case 0	321 758
Case G	322 194
Case P	962 702
Case V	323 358

In all four simulated cases, relatively small pressure drops are recorded, ranging from 21 kPa to 24 kPa, which have a negligible impact on the compression costs of the incoming gas flow.

Focusing on *Case V*, it can be observed that an increase in velocity results in a higher pressure drop compared to *Case 0*, albeit the difference being only 1.6 kPa. This results is consistent with the findings of Kunii et al. [20]. Indeed, observing the diagram in Figure 5.4, it can be noticed that beyond the minimum fluidization velocity u_{mf}, a progressive increase in velocity leads to a slight rise in pressure drops. This trend ends once a terminal velocity is reached, beyond which pneumatic transport of the entire bed occurs.

An increase in pressure drops is also observed when using sand grains with a larger diameter, as smaller solid particles require less pressure to be

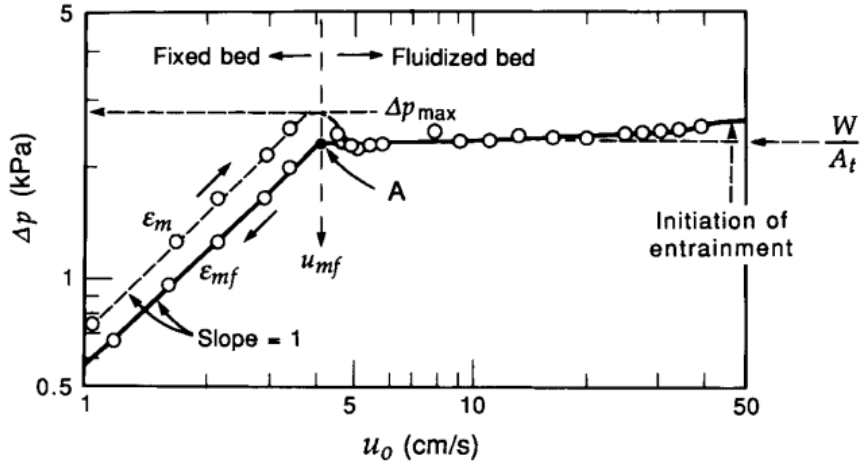

Figure 5.4: Pressure drops as a function of velocity for uniformly sized sand grains [20].

lifted [58].

Finally, an increase in operating pressure also leads to an increase in pressure losses along the riser axis. This result is consistent with findings by Dong et al. [59], who, however, highlighted a discrepancy between the results obtained through CFD simulations and those obtained experimentally, which demonstrate an opposite trend when pressure is increased. This discrepancy remains unclear but is likely related to the choice of model used to describe the drag force. In addition to being a function of pressure, the drag force is also a function of gas and particle velocity, and it may require modifications when it is used at higher pressures.

From Figure 5.3, it is noticeable that the trend of pressure drops in all cases leads to the distinction of two different zones. The first zone, at the bottom of the gasifier, exhibits a highly accentuated pressure drop gradient, while the section at the top of the riser maintains almost constant pressure. These two distinct zones correspond to the dense region, where there is a significant presence of the solid fraction, and the dilute region, where the solid particle fraction is considerably lower. The separation limit of the two regions depends on the magnitude of the drag force. It can be observed that an increase in pressure, resulting in a higher gas density, increases the magnitude of the drag force, as well as the injection of a gas stream at higher velocities. On the other hand, an increase in the diameter of solid particles leads to a shorter dense region, which witnesses the negative impact of this operating condition on the drag force magnitude.

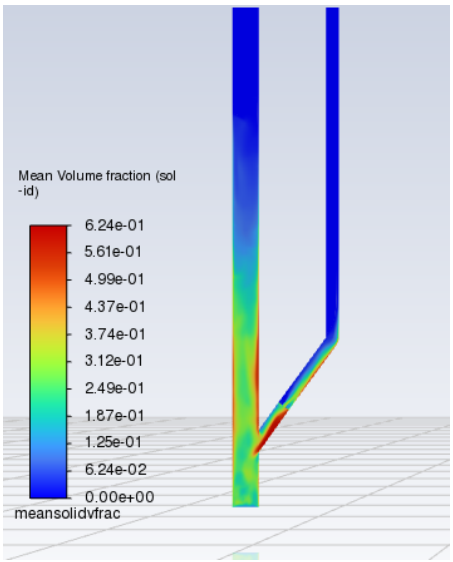

(a) Case 0

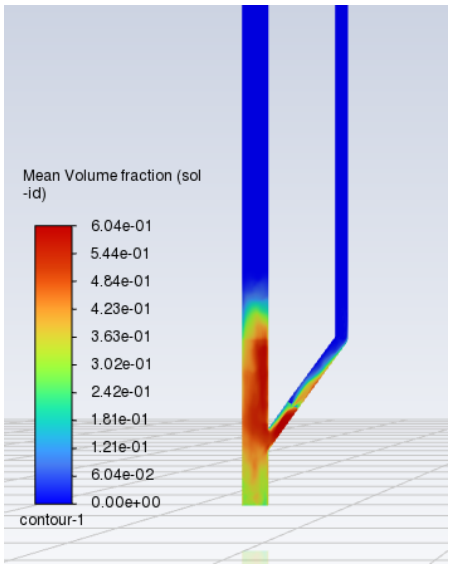

(b) Case G

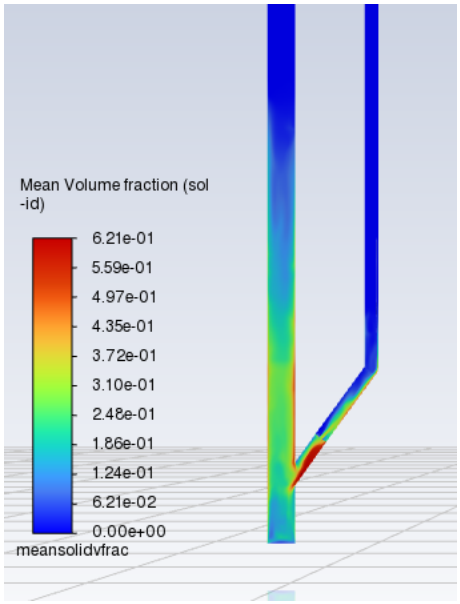

(c) Case P

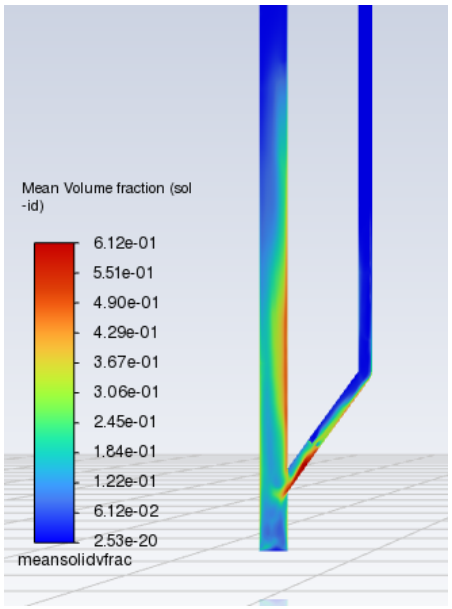

(d) Case V

Figure 5.5: Time-averaged solid volume fraction - Front View.

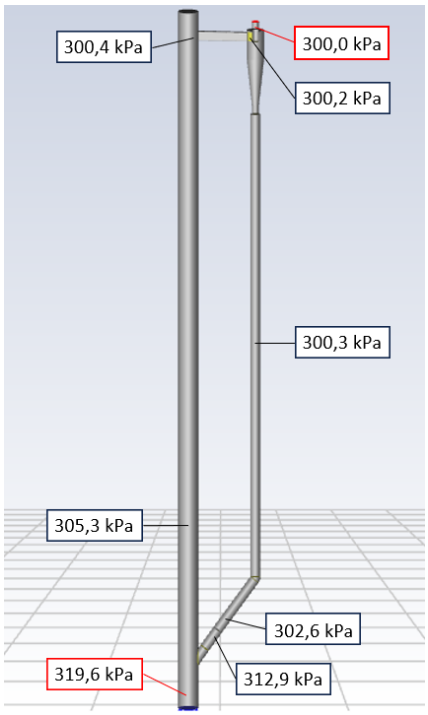

(a) Case 0

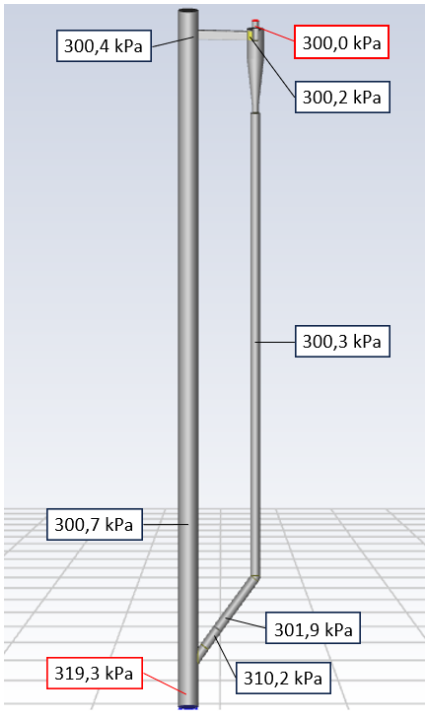

(b) Case G

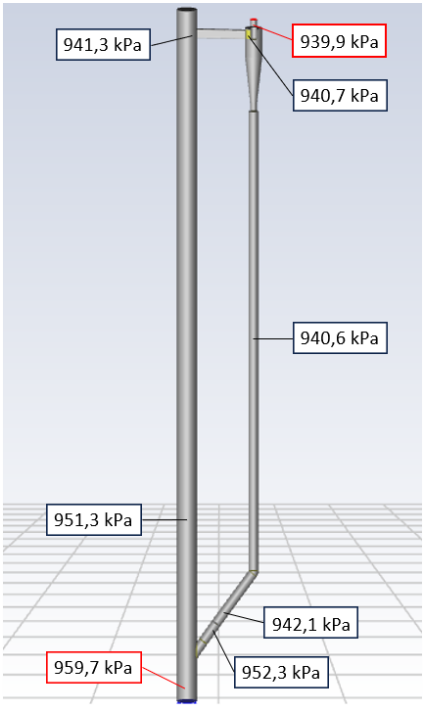

(c) Case P

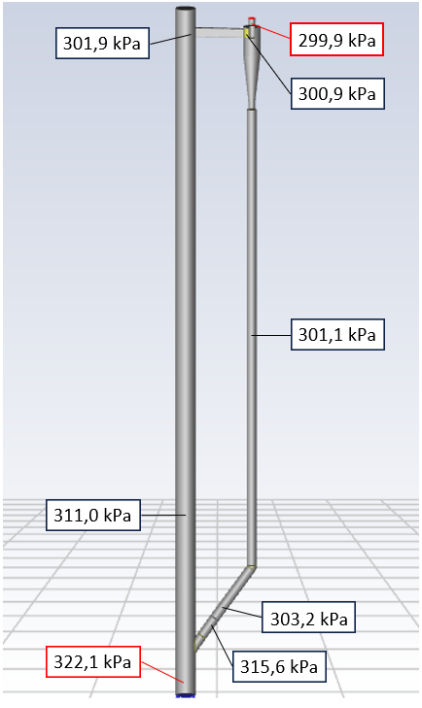

(d) Case V

Figure 5.6: "Pressure Loops".

Figure 5.5 provides a clearer image of the fluidized bed height in the models considered. From this image, it can also be observed how the orifice obstructs the rise of the solid fraction along the standpipe in all four cases during the first 5 seconds of activity. Thus, the effect of the different drag forces is more visibly apparent only along the riser of the gasifier.

In addition to analysing pressure drops along the vertical axis of the riser, it is interesting to observe the magnitude of the time-averaged pressure at various points throughout the entire gasifier. From Figure 5.6, it can be observed that in all four cases, there is a significant pressure drop because of the presence of the orifice, where there is a narrowing of the standpipe section. The greatest pressure difference between one side and the other of the metal surface is 12 kPa and occurs in *Case V*, when the gas has a higher velocity. A lower pressure drop is observed when the gas moves toward the obstruction at a lower velocity, i.e., when larger solid particles are used.

A similar behaviour is also observed when sampling the pressure on the two opposite sides of the channel connecting the riser and the cyclone. In *Case V*, pressure drops of 1 kPa are observed, which decrease to approximately 0.2 kPa in *Case 0* and *Case G*.

Some final considerations are made regarding the impact of the simplifications adopted during the modelling step.

A primary assessment concerns the reliability of the results by defining the fluid phase with constant viscosity and density. While the air viscosity changes imperceptibly with a pressure change on the order of 20 kPa, the fluid density varies more significantly in different parts of the gasifier. However, in light of the density values reported in Table 5.6, it is deemed appropriate to simplify by defining the fluid density with an intermediate value between those reported at 3 *bar* and 3.2 *bar* and between 9.4 *bar* and 9.6 *bar* in the lower and higher-pressure cases respectively.

A second aspect to consider is the absence of the gas distributor. Kunii and Levenspiel [20] mentioned how pressure drops due to the distributor can be estimated using a simple "rule of thumb":

$$\Delta P_d = (0.2 \ - \ 0.4)\Delta P_b \tag{5.1}$$

where ΔP_d is the pressure drop across the gas distributor $[Pa]$ and ΔP_b is the pressure drop inside the fluidized bed $[Pa]$.

Therefore, it can be observed that the absence of a distributor underestimates the pressure drops inside the gaifier, as the flow of fluid through the distributor can cause a pressure drop of up to 40% of the calculated pressure drop due to the bed inventory.

Table 5.6: Density of air at different pressures.

Density of air at lower pressures	
3.0 *bar*	3.56 kg/m^3
3.1 *bar*	3.68 kg/m^3
3.2 *bar*	3.81 kg/m^3
Density of air at higher pressures	
9.4 *bar*	11.17 kg/m^3
9.5 *bar*	11.29 kg/m^3
9.6 *bar*	11.41 kg/m^3

5.4 Analysis of solid volume fractions

To study the hydrodynamics of the simulated models, it is important to also focus on the distribution of the solid fraction within the reactor. Achieving efficient gasification requires a good degree of mixing with a homogeneous distribution of the solid fraction both radially and axially [59]. Referring to Figure 5.5, it is therefore crucial to operate under conditions that minimize the separation between the dense region and the dilute region. In this regard, it can be observed that an increase in pressure and velocity play a favourable role. The same cannot be said for an increase in particle size, which does not result in a good dispersion of solids along the height of the riser.

This result is confirmed by focusing on Figure 5.7, which depicts the volume fraction of solids, averaged over the sampled 5 seconds, along the section of the riser at a height of 1.5 meters. In *Case G*, a high concentration of solids is observed in this section of the gasifier, indicating that the entire solid fraction is solely concentrated in the lower portion of the gasifier and is not homogeneously distributed in height.

In the remaining cases, a characteristic core-annular flow structure is observed, with a high percentage of solids along the vessel walls and a more dilute region in the core. This discrepancy is more pronounced in *Case V*, where there is a high solid fraction adjacent to the wall contiguous to the junction with the standpipe.

Comparing both the front view and the top view of the solid distribution in *Case 0* and *Case P*, it is evident that an increase in pressure enhances particle mixing both axially and radially. However, even in *Case P*, a higher concentration of sand remains near the reactor walls. Similar findings were obtained by Dong et al. [59] in their research.

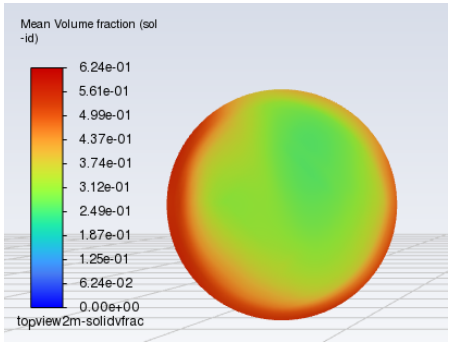

(a) Case 0

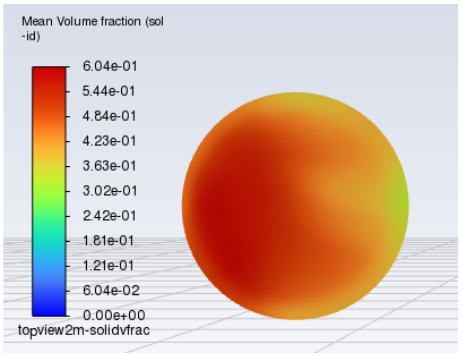

(b) Case G

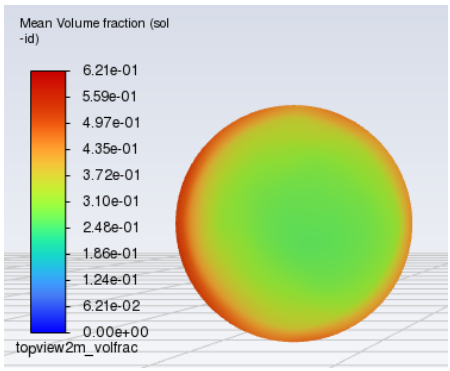

(c) Case P

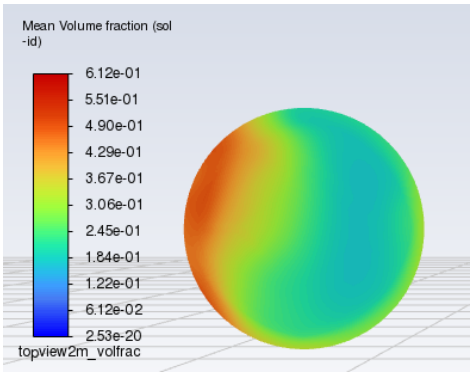

(d) Case V

Figure 5.7: Time-averaged solid volume fraction in the riser at a height of 1.5 meters - Top View.

5.5 Analysis of gas bypass

During the initial seconds of operation, the incoming gas ascends not only the riser, where gasification reactions occur, but also along the standpipe. This portion of gas represents a loss that directly mixes with the product gas at the exit of the gasifier. The gas bypass along the standpipe is a phenomenon that is desired to be reduced, given the high production costs of pure oxygen, which, along with air, is supplied to the gasification unit during normal operating conditions. It is therefore of interest in the current study to predict the influence of pressure, gas velocity, and sand grain size on the gas bypass.

The analysis has been performed by measuring the mass flow rate of gas passing through the orifice at a predefined time, in this case, at 5 seconds, and comparing this flow rate with the total mass flow rate entering the reactor.

Based on the results obtained, it is evident that the bypass of the gasifying

Table 5.7: Gas bypass along the standpipe.

	Mass flow rate of gas at the inlet [kg/s]	**Mass flow rate of gas through the orifice [kg/s]**	**Bypass [%]**
Case 0	0.181	0.036	19.9
Case G	0.181	0.063	35.0
Case P	0.362	0.019	30.8
Case V	0.565	0.174	5.2

agent is notably significant across all four cases. The flow of gas through the standpipe is attributed to the minimal presence of solids within this passage, primarily due to the obstructive nature of the orifice. However, upon a detailed examination of Table 5.7, it becomes clear that an increase in gas inlet velocity significantly diminishes the volume of gas entering the standpipe. Conversely, the most unfavourable scenario is observed with an increase in the diameter of solid particles, resulting in a bypass rate of up to 35%. Additionally, an increase in operating pressure also leads to a worsening in this regard.

5.6 Analysis of pressure fluctuations

One final aspect to be analysed within this discussion to capture the hydrodynamics of the system is the pressure fluctuations within the gasifier. It is acknowledged that the pressure signal in a certain location of the reactor arises from a combination of localized fluctuations, primarily caused by moving gas bubbles and rapidly propagating pressure waves resulting from bubble formation, coalescence, and eruption [60].

In the four cases examined, pressure has been sampled at a distance of 0.3 meters from the inlet, and it has been subsequently plotted as a function of time to highlight the absolute pressure fluctuations (i.e., the pressure fluctuations obtained by sampling a single point inside the reactor). From the results, as depicted in Figure 5.8, it is evident that all models exhibited a significant pressure peak at the start of the simulation. This finding leads to preliminary considerations regarding the physical stability of the reactor itself. During the reactor design phase, the engineer must consider potential pressure peaks that occur during critical phases, like the start-up and the shut-down of the process. According to European regulation EN 13445 for

unfired pressure vessels, the gasifier must be designed with thicknesses able to ensure stability even under exceptional operating conditions. However, it is important to emphasize how this kind of overpressure inside the gasifier is primarily mitigated by the presence of a gas distributor [20], and how, in the event of critical operating conditions, a ramp-up of gas inlet flow can be performed [61].

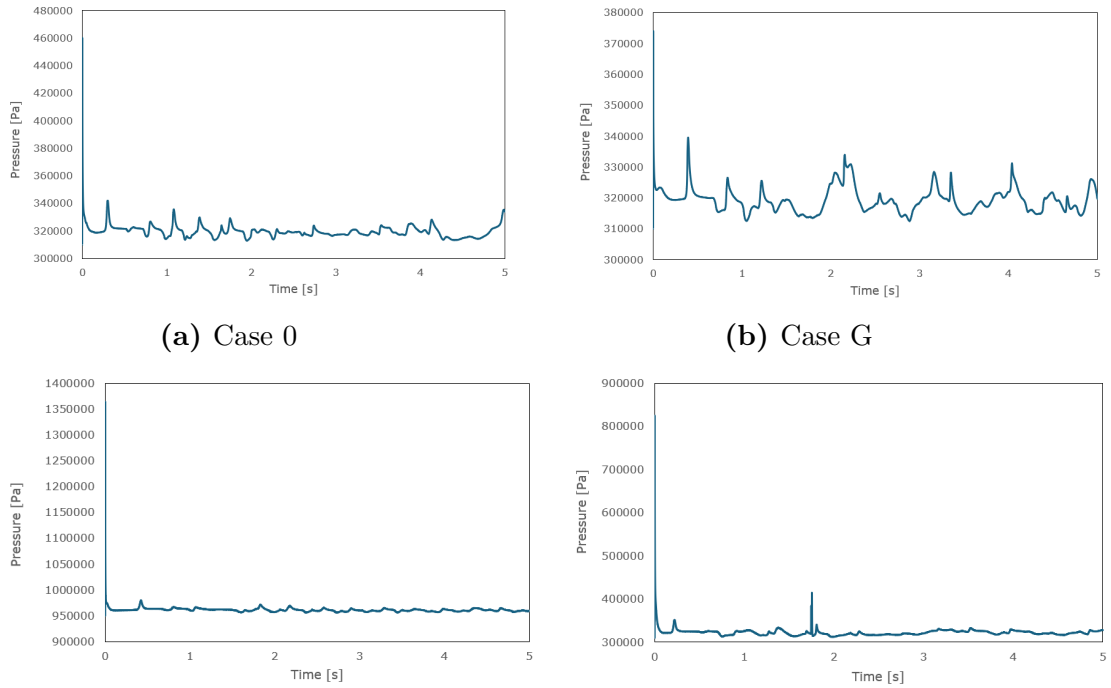

(a) Case 0 **(b)** Case G

(c) Case P **(d)** Case V

Figure 5.8: Pressure fluctuations in the riser at a height of 0.3 meters.

The overall trend of pressure fluctuations over time is influenced by various factors and operative conditions, such as particle geometry, gas pressure and velocity, and the location within the reactor where measurements are taken. To relate the sampled fluctuations to the study of hydrodynamics, statistical parameters, like the standard deviation σ_P $[Pa]$ of these fluctuations, are typically used:

$$\sigma_P = \sqrt{\frac{1}{N-1}\sum_{i=1}^{N}(P_i - \overline{P})^2} \tag{5.2}$$

N represents the number of sampled time steps $[-]$, P_i is the pressure

sampled at the i^{th} time step $[Pa]$, and $\overline{P}$ is the mean pressure $[Pa]$, defined as follows:

$$\overline{P} = \frac{1}{N} \sum_{i=1}^{N} P_i \tag{5.3}$$

Standard deviations of absolute pressure fluctuations can be used to determine the minimum fluidization velocity u_{mf} $[m/s]$ of the fluidized bed at specific pressure and temperature conditions. According to Puncochar et al. [62], u_{mf} can be derived by sampling pressure fluctuations and studying the standard deviation trends as a function of fluid inlet velocity u. Moreover, the result is not influenced by the sampling height, provided that the sampling is not done too close to the inlet section. In this regard, the analysis utilizes results obtained at 0.3 m from the inlet for both *Case 0* and *Case V*. The selection of these two cases is based on choosing scenarios with constant pressure (3 bar) and identical particle size (particle diameter equal to 250 μm). An additional case was simulated for analysis, characterized by the same pressure and particle size, and an inlet gas velocity of 0.6 m/s.

It is possible to perform a linear regression analysis on the obtained data and achieve similar outcomes to the conclusions drawn by Puncochar et al. [62], who showed that σ_P is a linear function of the gas velocity:

$$\sigma_P = A + Bu \tag{5.4}$$

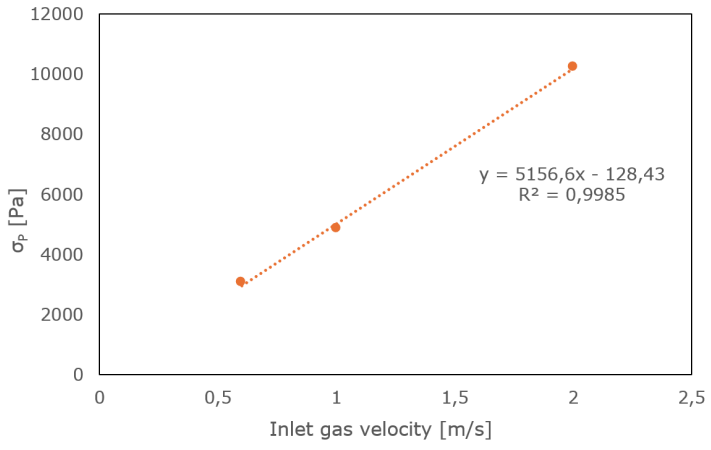

Figure 5.9: Linear regression of standard deviations.

The absence of any standard deviation, indicating no movement of solids or presence of bubbles within the bed, aligns with the minimum fluidization velocity. Therefore,

$$u_{mf} = -\frac{A}{B} = 0.025\,\frac{m}{s} \tag{5.5}$$

Nevertheless, the obtained result reveals a significant disparity between the minimum fluidization velocity and the velocities of interest, with the latter being 40-80 times higher. The attention is thus directed towards identifying the fluidization regime of the case studies, and this information can be inferred from analyzing the standard deviations of the differential pressure fluctuations.

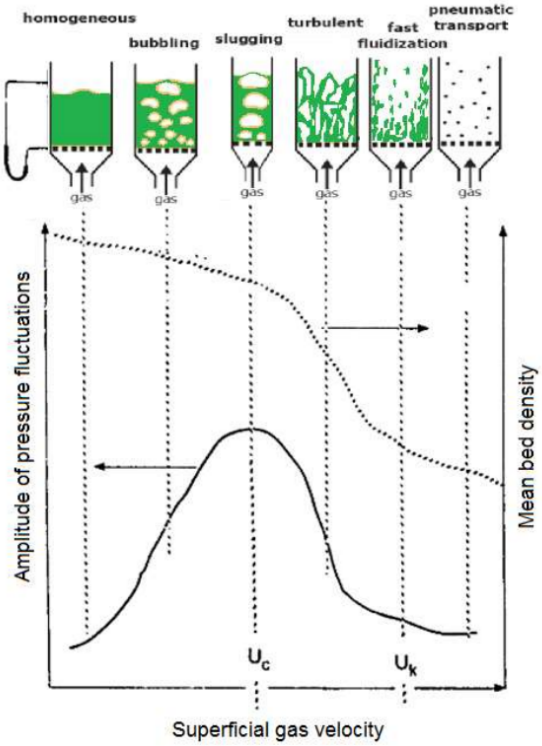

Figure 5.10: Standard deviation of differential pressure fluctuations for fluidization regime determination [63].

This study involves measuring the pressure at two different heights of the gasifier and deriving the standard deviations of pressure differences between the two sampling points. In Figure 5.10, it can be observed that, at constant pressure and particle size, an increase in operating velocity leads to

an increase in the standard deviations of pressure fluctuations, attributed to the presence of bubbles forming at the reactor inlet and moving through the solid bed. This trend ceases upon reaching the slugging condition, where it becomes impossible to identify gas bubbles rising uniformly along the fluidized bed, but instead irregular gas voids ascend with markedly turbulent motion. Further increasing the fluid velocity allows the gas to more effectively entrain solid particles upward. Consequently, the pressure fluctuations between two sampled points become less significant, eventually reaching a new state of homogeneity where complete pneumatic particle transport upward occurs, and the standard deviations of differential pressure fluctuations tend towards values closer to zero.

In the current study, the sampled points are located respectively at 0.3 m and 2 m from the inlet section for all examined cases. Due to the significant distance between the two sampling points, a velocity-σ_P graph comparable to that obtained by plotting the standard deviations of absolute pressure fluctuations is obtained, as shown in Figure 5.11. Furthermore, in order to achieve a result similar to that plotted in Figure 5.10, numerous other cases at different gas inlet velocities need to be simulated.

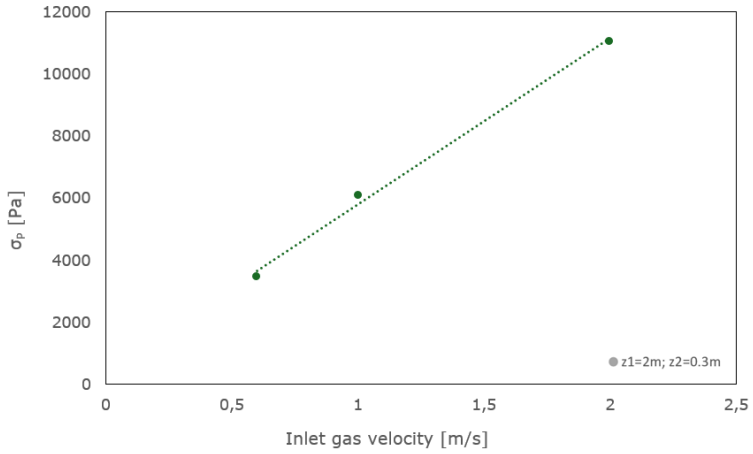

Figure 5.11: Standard deviation of differential pressure fluctuations with pressure probes at 0.3 m and 2 m.

The fluidization regimes of the fluidized beds are therefore qualitatively evaluated by analysing some frames captured in the various cases, by sectioning the gasifier with the plane $z = 0$. Moreover, the classification of the regime of fluidization inside the gasifier references Kunii and Levenspiel in *Fluidization Engineering - Second Edition* [20].

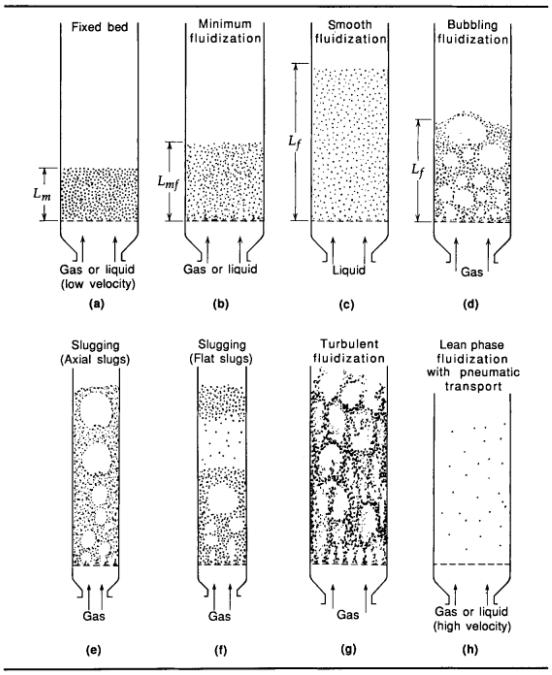

Figure 5.12: Fluidization regimes [20].

Starting focusing on *Case P* and *Case V* in Figure 5.13, it is possible to see how at these conditions the presence of bubbles is not further recognizable. In both cases, there is an exceeding of the terminal velocity, under their respective pressure conditions, beyond which most particles are entrained. There is no longer a distinct upper surface of the fluidized bed, and, as discussed in Paragraph 5.3, there is a better distribution of particles along the riser axis. In accordance with Figure 5.12,the fluidization regime of the two cases reflects a transitional state between a turbulent fluidization and lean phase fluidization. In this state of fluidization, the presence of a cyclone to collect the particles carried by the gas stream is therefore necessary.

On the other hand, in *Case 0* and in *Case G*, the bed upper surface is still distinguishable, but voids of gas of irregular shapes and turbulent motion of the solid phase are more noticeable than clearly distinguishable rising bubbles. Referring to Figure 5.12, it can be concluded that these two cases exhibit a fluidization regime that lies between a slugging and a turbulent fluidization regime.

At the end of this analysis, it is important to emphasize that the absence of bubbles, and therefore the fluidization regime of all the cases discussed, is significantly influenced by the absence of the gas distributor at the reactor inlet.

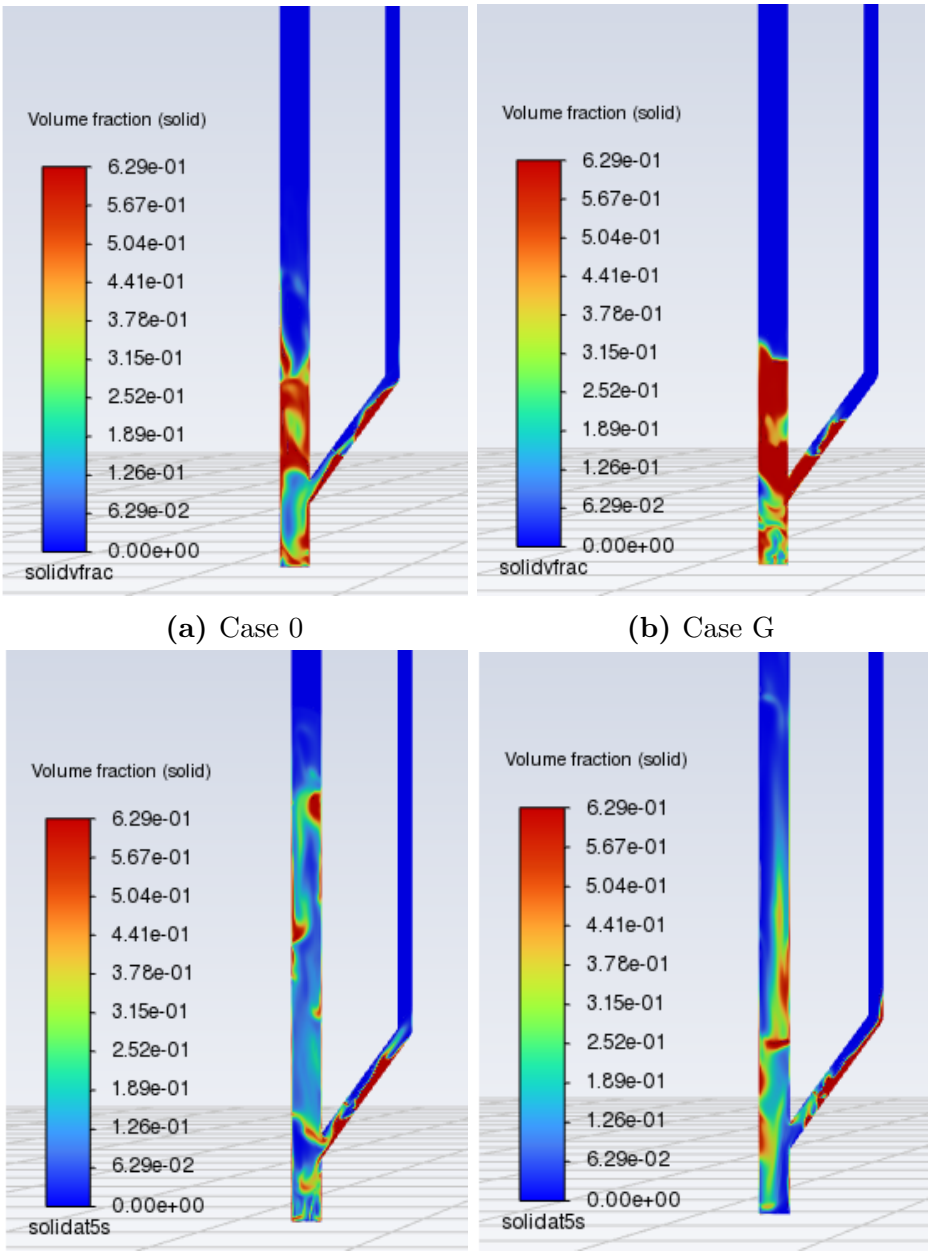

(a) Case 0 **(b)** Case G

(c) Case P **(d)** Case V

Figure 5.13: Snapshots of the solid volume fraction at 5 seconds.

Chapter 6

Conclusions

In the hydrodynamic study performed, a reference case was simulated, and the effect of pressure, gas inlet velocity, and particle size was studied by modelling three additional cases, each modifying only one of the aforementioned operating conditions.

A first result shows that an increase in gas inlet velocity leads to higher pressure drops, but improves the overall mixing quality. A higher density region provides greater axial homogeneity, while radial homogeneity can be tested by simulating the model over a longer period. Moreover, the bypass of the gasifying agent is significantly reduced at higher gas velocity. Finally, this scenario results in a fluidization regime potentially involving significant solid particles transport, necessitating the presence of a cyclone for their recirculation.

Similarly, an increase in pressure causes higher pressure drops, along with a clear improvement in mixing quality, both axially and radially. However, higher pressures require greater structural stability precautions for the gasifier, given the more pronounced difference between internal and external pressures. Moreover, higher operating pressure accentuates the phenomenon of bypass along the standpipe of the gasifier. Analogously to a system with high inlet gas velocity, increased pressure necessitates a solid phase recirculation system due to the higher gas density and consequently, an increased drag force.

On the other hand, increasing the diameter of particles used as heat carrier does not improve hydrodynamics. A slight increase in pressure losses has been recorded compared to the base case, and mixing quality is negatively affected. Bypass of the air-oxygen mixture is also improved by the presence of more voluminous particles. Nonetheless, pronounced turbulence occurs in the fluidized bed, characterized not by distinct bubbles but by irregular gas voids and solid clusters.

To improve the quality of the results, it is advisable to repeat the simulations while considering the presence of a gas distributor. Its absence underestimates pressure drops within the system and compromises the identification of the fluidization regime in the various cases studied. Additionally, it is advisable to conduct simulations for longer periods as a pseudo-steady state is reached only after 1 or 2 minutes of operation. Furthermore, an extended simulation time can help predict any solid presence at the gasifier outlet. Finally, to enhance the reliability of the results, it is also possible to examine scenarios that take into account the particle size distribution of the sand used, as well as cases where the inlet gas velocity is gradually increased to a target velocity.

Bibliography

[1] World Metorological Organization. *WMO update: 50:50 chance of global temperature temporarily reaching 1.5˚C threshold in next five years*, 2022. URL https://public.wmo.int/en/media/press-release/wmo-update-5050-chance-of-global-temperature-temporarily-reaching-15%C2%B0c-threshold.

[2] European Council. *European Green Deal*, Accessed: 13th September 2023. URL https://www.consilium.europa.eu/en/policies/green-deal/#what.

[3] European Commission. *REPowerEU: A plan to rapidly reduce dependence on Russian fossil fuels and fast forward the green transition*, Accessed: 13th November 2023. URL https://ec.europa.eu/commission/presscorner/detail/en/ip_22_3131.

[4] A. Loppinet-Serani, C. Aymonier, and F. Cansell. *Current and Foreseeable Applications of Supercritical Water for Energy and the Environment. ChemSusChem*, 2008. doi: 10.1002/cssc.200700167.

[5] International Energy Agency (IEA). *Bioenergy*, Accessed: 13th November 2023. URL https://www.iea.org/energy-system/renewables/bioenergy.

[6] P. Basu. *Biomass Gasification and Pyrolysis: Practical Design and Theory.* Academic Press, 2010.

[7] J. G. Speight. *Gasification of Unconventional Feedstocks.* Gulf Professional Publishing, 2014.

[8] R. J. LeBlanc. *Black Liquor Gasification Can Help Sustain Forests, Generate Ultra-Clean Biofuels. Biomass Magazine*, 2009.

[9] A. Ernsting. *Biomass gasification & pyrolysis: How UK support for 'energy innovation' leads to business failures and particularly inefficient and dirty biomass power stations. biofuelwatch*, 2015.

[10] Bio-FlexGen. *Bio-FlexGen - Making the Green Deal real!*, Accessed: 18th September 2023. URL `https://bioflexgen.eu/`.

[11] E. Dahlquist, K. Engvall, and T. Liliedahl. *Technologies for Converting Biomass to Useful Energy*. CRC Press, 2013.

[12] D. Mohan, C. U. Pittman Jr., and P. H. Steele. *Pyrolysis of Wood/Biomass for Bio-oil: A Critical Review. Energy Fuels*, 2006. doi: 10.1021/ef0502397.

[13] A. Molino, S. Chianese b, and D. Musmarra. *Biomass gasification technology: The state of the art overview. Journal of Energy Chemistry*, 2015. doi: 10.1016/j.jechem.2015.11.005.

[14] P. Simell, E. Kurkela, and P. Ståhlberg. *Formation and Catalytic Decomposition of Tars from Fluidized-Bed Gasification*. 1993. doi: 10.1007/978-94-011-1336-6_20.

[15] H. Knoef. *Handbook Biomass Gasification*. BTG, 2005.

[16] W. Chen, J. Peng, and X. T. Bi. *Operating parameter effects on the solids circulation rate in the CFD simulation of a dual fluidized-bed gasification system. Chemical Engineering Science*, 2016. doi: 10.1016/j.ces.2016.11.040.

[17] Ö. Tezer, N. Karabag, C. Ö. Çolpan, and A. Ayol. *Biomass gasification for sustainable energy production: A review. International Journal of Hydrogen Energy*, 2022. doi: 10.1016/j.ijhydene.2022.02.158.

[18] S. Mishra and R. K. Upadhyay. *Review on biomass gasification: Gasifiers, gasifying mediums, and operational parameters. Materials Science for Energy Technologies*, 2021. doi: 10.1016/j.mset.2021.08.009.

[19] M. J. Khan and K. A. Al-attab. *Steam Gasification of Biomass for Hydrogen Production – A Review and Outlook. Journal of Advanced Research in Fluid Mechanics and Thermal Sciences*, 2022. doi: 10.37934/arfmts.98.2.175204.

[20] D. Kunii and O. Levenspiel. *Fluidization Engineering - Second Edition*. Butterworth-Heinemann, 1991.

[21] Phoenix BioPower. *Our Technology - HFB gasifier*, Accessed: 29th November 2023. URL `https://phoenixbiopower.com/the-hfb-gasifier-1`.

[22] D. Geldart. *Types of Gas Fhidization. Powder Technology*, 1973. doi: 10.1016/0032-5910(73)80037-3.

[23] R. Cocco and J. W. Chew. *50 years of Geldart classification. Powder Technology*, 2023. doi: 10.1016/j.powtec.2023.118861.

[24] Q. Guo, Y. Liu, and M. Wang. *Fluidization Characteristics of Printed Circuit Board Plastic Particles With Different Sizes. The Canadian Journal of Chemical Engineering*, 2010. doi: 10.1002/cjce.20345.

[25] J. Marinkovic, H. Thunman, P. Knutsson, and M. Seemann. *Characteristics of olivine as a bed material in an indirect biomass gasifier. Chemical Engineering Journal*, 2015. doi: 10.1016/j.cej.2015.05.061.

[26] F. Kirnbauer and H. Hofbauer. *The mechanism of bed material coating in dual fluidized bed biomass steam gasification plants and its impact on plant optimization. Powder Technology*, 2013. doi: 10.1016/j.powtec.2013.04.022.

[27] X. Meng, W. de Jong, N. Fu, and A. H. M. Verkooijen. *Biomass gasification in a 100 kWth steam-oxygen blown circulating fluidized bed gasifier: Effects of operational conditions on product gas distribution and tar formation. Biomass and Bioenergy*, 2011. doi: 10.1016/j.biombioe.2011.03.028.

[28] T. Berdugo Vilches, J. Maric, P. Knutsson, D. C. Rosenfeld, H. Thunman, and M. Seemann. *Bed material as a catalyst for char gasification: The case of ash-coated olivine activated by K and S addition. Fuel*, 2018. doi: 10.1016/j.fuel.2018.03.079.

[29] Y. Guan, J. Chang, K. Zhang, B. Wang, and Q. Sun. *Three-dimensional CFD simulation of hydrodynamics in an interconnected fluidized bed for chemical looping combustion. Powder Technology*, 2014. doi: 10.1016/j.powtec.2014.08.046.

[30] ANSYS Inc. *Ansys Fluent Theory Guide*. 2022.

[31] D. Gidaspow. *Multiphase Flow and Fluidization - Continuum and Kinetic Theory Descriptions*. Academic Press, 1994.

[32] M. Syamlal and T. J. O'Brien. *Simulation of granular layer inversion in liquid fluidized beds. International Journal of Multiphase Flow*, 1988. doi: 10.1016/0301-9322(88)90023-7.

[33] N. Yang, W. Wang, W. Ge, and J. Li. *CFD simulation of concurrent-up gas–solid flow in circulating fluidized beds with structure-dependent drag coefficient. Chemical Engineering Journal*, 2003. doi: 10.1016/j.cej.2003.08.006.

[34] M. Upadhyay and J. Park. *CFD simulation via conventional Two-Fluid Model of a circulating fluidized bed riser: Influence of models and model parameters on hydrodynamic behavior. Powder Technology*, 2014. doi: 10.1016/j.powtec.2014.12.011.

[35] H. Zhong, J. Gao, C. Xu, and X. Lan. *CFD modeling the hydrodynamics of binary particle mixtures in bubbling fluidized beds: Effect of wall boundary condition. Powder Technology*, 2012. doi: 10.1016/j.powtec.2012.07.037.

[36] C. Zi, J. Sun, Y. Yang, Z. Huang, Z. Liao, J. Wang, Y. Yang, and G. Han. *CFD simulation and hydrodynamics characterization of solids oscillation behavior in a circulating fluidized bed with sweeping bend return. Chemical Engineering Journal*, 2016. doi: 10.1016/j.cej.2016.08.127.

[37] S. Yin, W. Zhond, B. Jin, and J. Fan. *Modeling on the hydrodynamics of pressurized high-flux circulating fluidized beds (PHFCFBs) by Eulerian–Lagrangian approach. Powder Technology*, 2014. doi: 10.1016/j.powtec.2014.03.059.

[38] L. Wei, W. Yen, and Z. Luo. *A preliminary CFD study of the gas–solid flow fields in multizone circulating polymerization reactors. Powder Technology*, 2011. doi: 10.1016/j.powtec.2011.08.005.

[39] C. Dinh, S. Hsiau, C. Su, M. Tsai, Y. Chen, H. Nguyen, and H. Wan. *Predictions of undesirable air–sand flow behaviors in a dual fluidized bed cold flow system via a CFD full-loop model. Journal of the Taiwan Institute of Chemical Engineers*, 2019. doi: 10.1016/j.jtice.2019.11.001.

[40] Z. Wan, J. Hu, and X. Qi. *Numerical analysis of hydrodynamics and thermochemical property of biomass gasification in a pilot-scale circulating fluidized bed. Energy*, 2021. doi: 10.1016/j.energy.2021.120254.

[41] S. Ergun. *Fluid flow through packed columns. Chemical Engineering Progress*, 1952.

[42] C. Y. Wen and Y. H. Yu. *A generalized method for predicting the minimum fluidization velocity. AlChE Journal*, 1966.

[43] H. Lu, D. Gidaspow, and S. Wang. *Computational Fluid Dynamics and the Theory of Fluidization*. Springer Nature Singapore Pte Ltd., 2021.

[44] J. Ding and D. Gidaspow. *A Bubbling Fluidization Model Using Kinetic Theory of Granular Flow. AlChE Journal*, 1990. doi: 10.1002/aic.690360404N.

[45] C. K. K. Lun, S. B. Savage, D. J. Jeffrey, and N. Chepurniy. *Kinetic theories for granular flow: Inelastic particles in Couette flow and slightly inelastic particles in a general flowfield. Journal of Fluid Mechanics*, 1984. doi: 10.1017/S0022112084000586.

[46] R. Rorato, M. Arroyo, E. Andò, and A. Gens. *Sphericity measures of sand grains. Engineering Geology*, 2019. doi: 10.1016/j.enggeo.2019.04.006.

[47] S. Pecate, M. Morin, S. A. Kessas, M. Hemati, Y. Kara, and S. Valin. *Hydrodynamic study of a circulating fluidized bed at high temperatures: Application to biomass gasification. KONA Powder and Particle Journal*, 2018. doi: 10.14356/kona.2019018.

[48] D. Gidaspow, R. Bezburuah, and J. Ding. *Hydrodynamics of Circulating Fluidized Beds, Kinetic Theory Approach. Fluidization VII, Proceedings of the 7th Engineering Foundation Conferenceon Fluidization*, 1992.

[49] M. Syamlal, W. Rogers, and T. J. O'Brien. *MFIX documentation theory guide*. 1993. doi: 10.2172/10145548.

[50] D. G. Schaeffer. *Instability in the evolution equations describing incompressible granular flow. Journal of Differential Equations*, 1985. doi: 10.1016/0022-0396(87)90038-6.

[51] F. Moukalled, L. Mangani, and M. Darwish. *The Finite Volume Method in Computational Fluid Dynamics - An Advanced Introduction with OpenFOAM® and Matlab®*. Springer, 2016.

[52] B. Andersson, R. Andersson, L. Håkansson, M. Mortensen, R. Sudiyo, and B. van Wachem. *Computational Fluid Dynamics for Engineers*. Cambridge University Press, 2012.

[53] J.Tu, G. Yeoh, and C. Liu. *Computational Fluid Dynamics - A Practical Approach. 2nd Edition*. Elsevier Ltd., 2013.

[54] ANSYS Inc. *ANSYS FLUENT 12.0 User's Guide*. 2009.

[55] T. Li, J. Grace, and X. Bi. *Study of wall boundary condition in numerical simulations of bubbling fluidized beds. Powder Technology*, 2010. doi: 10.1016/j.powtec.2010.06.005.

[56] C. Dinh, S. Hsiau, C. Su, M. Tsai, Y. Chen, H. Nguyen, and H. Wan. *Full-loop study of a dual fluidized bed cold flow system: Hydrodynamic simulation and validation. Advanced Powder Technology*, 2021. doi: 10.1016/j.apt.2021.01.012.

[57] D. W. Green and M. Z. Southard. *Perry's Chemical Engineers' Handbook - 9th Edition.* McGraw-Hill Education, 2019.

[58] E. Yohana, Muchammad, M. Tauviqirrahman, A. A. Sayekti, K. Hwan-Choi, and V. Paramita. *Effect of particle size and bed height on the characteristic of a fluidized bed dryer. Cogent Engineering*, 2020. doi: 10.1080/23311916.2020.1738185.

[59] P. Dong, Q. Tu, H. Wang, and Z. Zhu. *Effects of pressure on flow characteristics in a pressurized circulating fluidized bed. Particuology*, 2021. doi: 10.1016/j.partic.2020.07.004.

[60] C. Sobrino, S. Sánchez-Delgado, N. García-Hernando, and M. de Vega. *Standard deviation of absolute and differential pressure fluctuations in fluidized beds of group B particles. Chemical Engineering Research and Design*, 2008. doi: 10.1016/j.cherd.2008.06.006.

[61] M. Suárez-Almeida, A. Gómez-Barea, A.F. Ghoniem, S. Nilsson, and B. Leckner. *Modeling the transient response of a fluidized-bed biomass gasifier. Fuel*, 2020. doi: 10.1016/j.fuel.2020.117226.

[62] M. Puncochar, J. Drahos, J. Cermak, and K. Selucky. *Evaluation of minimum fluidizing velocity in gas fluidized bed from pressure fluctuations. Chemical Engineering Communications*, 1985. doi: 10.1080/00986448508911219.

[63] S. Specchia. *Multiphase Equipment Design course.* Politecnico di Torino, 2021.

.